Carbon Nanotube-based Field Ionization Vacuum Pump

ARCHIVES

by

Daniel Jang

B.S., E.E., M.I.T., 2010

Submitted to the Department of Electrical Engineering and Computer Science
in partial fulfillment of the requirements for the degree of

Master of Engineering in Electrical Engineering and Computer Science

at the

MASSACHUSETTS INSTITUTE OF TECHNOLOGY

June 2012

© Massachusetts Institute of Technology 2012. All rights reserved.

Author .....
Department of Electrical Engineering and Computer Science
March 5, 2012

Certified by .....
Dr. Luis Fernando Velásquez-García
Principal Research Scientist
Thesis Supervisor

Certified by .....
Prof. Akintunde Ibitayo (Tayo) Akinwande
Professor
Thesis Supervisor

Accepted by .....
Prof. Dennis M. Freeman
Masters of Engineering Thesis Committee

Carbon Nanotube-based Field Ionization Vacuum Pump

by

Daniel Jang

Submitted to the Department of Electrical Engineering and Computer Science
on March 5, 2012, in partial fulfillment of the
requirements for the degree of
Master of Engineering in Electrical Engineering and Computer Science

Abstract

We report the development of a novel micropump architecture that uses arrays of isolated vertical carbon nanotubes (CNT) to field ionize gas particles. The ionized gas molecules are accelerated to and implanted into a negatively biased getter removing the gas molecules from the volume being pumped.

CNTs are ideal for field ionization because of their nano-sized diameter, high aspect ratio and of their robust chemical and mechanical structure. The ionizing CNTs are biased at a much higher electrical potential than the gate material surrounding it. Because of the high aspect ratio of CNTs, the area near the tip of the ionizing CNT exhibits very high electric field strength. Gas molecules that are in close proximity to the CNT tips are ionized when electrons tunnel from the gas molecules to the CNT tips. A negatively biased getter positioned nearby attracts the ionized gas molecules, which are implanted in the getter material. With the gas molecules removed from the enclosed space, reduction of the pressure is achieved.

Key challenges in this Field Ionization Pump (FIP) project were the fabrication of high yield working pumps and a high enough ionization current at low voltages. The FIP is designed to evacuate volumes from low vacuum (30 Torr) to mid-vacuum (3 mTorr). We designed the device using electrostatic simulations. Several designs for the FIP ionizers were developed, and we created a device capable of producing field ionization current of 4 nA using an array of 96 field ionizers with 700 V bias voltage at $5 \cdot 10^{-5}$ Torr. We also show that ion implantation of the ionized atmospheric gas occurs in a silicon getter biased at 1000 V, which is confirmed via X-ray photoelectron spectroscopy (XPS).

Thesis Supervisor: Dr. Luis Fernando Velásquez-García
Title: Principal Research Scientist

Thesis Supervisor: Prof. Akintunde Ibitayo (Tayo) Akinwande
Title: Professor

Acknowledgments

First and foremost I'd like to thank Dr. Luis Fernando Velásquez-García for all of his dedication and care into guiding me throughout this project. Your expertise in fabrication processes was invaluable in getting this project moving so quickly, and your critical analysis helped me so much in honing my thought process. Thank you Prof. Ibitayo (Tayo) Akinwande for your guidance throughout my graduate student career and instilling in me the importance of looking at the big picture. Your excitement with all that is thought-provoking is very contagious, and I hope to never stop being curious at the world surrounding me.

I would like to thank the MTL staff members for always being helpful when I have faced hurdles in the processing and planning of the devices. I would like to thank my fellow group members Stephen and Vivi for helping me so much throughout my project. Thank you rest of the group members Michael, Annie, Melissa, Eric, Elle, Kerry, and Alex for your support and rapport — all of you have shown me what it means to be a scholarly student and how to continue to push myself forward.

Last but most definitely not least, I'd like to thank my mom, dad and my brother for always supporting me through the all the walks of my life. I always appreciate your support and advice as they are invaluable to me.

Contents

1 Introduction & Motivation **15**

1.1 Chip Scale Micro Vacuum Pump Project 15

1.2 Overview of the Ion Pumps 18

1.3 Thesis Organization 19

2 Background & Theory **21**

2.1 Theory of Field Ionization 21

2.2 Comparison to Electron Impact Ionization and Field Emission 25

3 Device Structure and Architecture **29**

3.1 Horse-shoe (co-planar) Design 30

3.2 Floral (layer-by-layer) Design 30

3.3 Self-aligned-gate Design 31

4 Device Modeling **33**

4.1 FEM Electrostatic Simulation 33

4.2 Estimation of the Tunneling Probability 36

4.3 Comparison to Previous Work 37

4.4 Pump Performance Calculations 40

5 Device Fabrication **45**

5.1 Horse-shoe (co-planar) Device Fabrication 45

5.2 Floral (layer-by-layer) Device Fabrication 49

5.3 Self-aligned-gate Device Fabrication 55

5.4 Discussion of the Fabrication Process 57

6 Electrical Characterization **61**

6.1 Field Emission Characterization 61

6.2 Field Ionization Characterization 64

7 Summary & Future Work **67**

7.1 Thesis Summary 67

7.2 Suggestions for Future Work 68

A Mask Layouts **71**

B Process Flows **75**

C Sensitivity Analysis of the Model **81**

D Electrical Characterization of the Horse-shoe Device (10-O) **83**

E Electrical Characterization of the Macro Device **87**

F MATLAB Code **95**

List of Figures

1-1 A schematic of the Chip Scale Micro Vacuum Pump project 17

2-1 A field ionization pump schematic 21

2-2 Potential well diagram of a molecule going through field ionization . . 22

2-3 Potential well diagram of an electron during field emission 26

3-1 Diagram of the horse-shoe design structure 30

3-2 Diagram of the floral device structure 31

3-3 Diagram of the self-aligned-gate device structure 32

4-1 Axisymmetric Maxwell SV Simulation of a CNT tip with a 30 nm radius with 2 μm aperture radius 34

4-2 Axisymmetric Maxwell SV Simulation of a CNT tip with a 20 nm radius and 0.4 μm aperture radius 35

4-3 Field strength dependence on distance from the tip for various tip radii 36

4-4 The ionization volume for various tip radii at 1000 V tip bias 37

4-5 MATLAB calculation of pump performance with various leak rates . 43

5-1 Summarized fabrication steps for the original horse-shoe design 46

5-2 SEM image of grooves etched on the a-Si layer 47

5-3 SEM images of Ni nanodots after patterning and etching 48

5-4 SEM images of CNT creation on the horse-shoe device 49

5-5 The result of arcing due to exposed oxide layer in the PECVD process for CNT growth 49

5-6 Summarized fabrication steps for the floral-design device 50

5-7 SEM images of a few pump sites after Ni and TiN etching steps . . . 52
5-8 SEM images of the floral device after CNT growth 52
5-9 SEM images of the oxide covered CNTs on the floral device 53
5-10 SEM images of the floral device after CMP 53
5-11 SEM image of the patterned n-a-Si gate layer 54
5-13 Summarized fabrication steps for the self-aligned-gate devices 56
5-14 SEM images of the self-aligned-gate devices 56
5-15 SEM images of hybrid etching method of Ni 57
5-16 SEM of an over-etched horse-shoe device during the XeF_2 release step 58
5-17 SEM of fabrication issues in the floral and self-aligned-gate structures 59

6-1 A sample electrical test setup 61
6-2 A picture of a device undergoing electrical testing 62
6-3 Field emission I-V curve for 10-O 63
6-4 The Fowler-Nordheim plot for 10-O 64
6-5 Field ionization I-V curve for 10-O 65

7-1 Schematic of a sample pump test setup 68
7-2 Test setup created for pump testing 69

A-1 Mask layout of the horse-shoe design: electrode layer 71
A-2 Mask layout of the horse-shoe design: nanodot catalyst layer 72
A-3 Mask layout of the hose-shoe design: all layers 72
A-4 The two different aperture radii for the gate structure in the mask layout 73

D-1 Comparison of currents during FE for 10-O 84
D-2 Noise test using the electrical test setup 85

E-1 SEM image of the CNT forrest growth 88
E-2 Macro test I-V curve of the FE test with the forrest CNTs 89
E-3 Comparison of the emitted current to the gate/getter current for the FE test with a forrest of CNTs 89
E-4 Fowler-Nordheim plot for the FE test with a forrest of CNTs 90

E-5 FI characterization of the forrest of CNTs 91
E-6 The discolored getter piece after the field ionization run 92
E-7 I-V curve for the macro FIP test with a forrest of CNTs 93

List of Tables

4.1 Extracted data from Chen's field ionization tests 38
4.2 Parameters used in estimating Chen's device performance for field ionization 39
4.3 Comparison of Chen's device performance estimation and experimental data 39
4.4 Sentivity analysis of the non-linear variables in the model 40

Chapter 1

Introduction & Motivation

1.1 Chip Scale Micro Vacuum Pump Project

Interest in vacuum electronics and their applications has increased in the recent past due to advances in high-frequency amplifiers [1], vacuum fluorescent displays [2], and a variety of sensors such as resonators, infrared sensors and mass spectrometers [3]. These devices require low pressure in order to have long mean free path for electron transport without collisions. Long mean free path is essential for device functionality, sensitivity, and reliability. As these technologies approach smaller scales, the devices find potential application in portable systems where low power consumption is of essence. In order to achieve this, the vacuum pump will also need to consume low power and be integrated with the vacuum electronic device.

In creating such vacuum pumps, several challenges are encountered, as many of the existing technologies are unsuitable for chip-scale integration and low power operation. The industry standard mechanical vacuum pump such as the turbomolecular pumps consume high amount of energy and are quite large as they use multiple stages of rotors in series that require high speeds. This is required in order to continually transfer momentum from the blades to the gas molecules even at low pressure where the mean free path is much longer. Mechanical roughing pumps have been miniaturized and have been shown to be successful though it is only able to attain low vacuum levels [4]. The mean free path is of the order of a few microns at this vacuum level,

which is close to the size of the pump chamber, and momentum transfer to the gas molecules is much more reduced resulting in almost no net pressure gradient. In order to achieve higher vacuum levels other technologies must be used. Non-mechancal vacuum pumps with no moving parts also exist such as Knudsen pumps and cryopumps. The Knudsen pump uses a thin channel with a temperature gradient to direct the flow of gas molecules and are micromachined into chip-scale levels; however, the demonstrated terminal pressure is only 0.48 atm [5]. The cryopump cools a surface to below 120 K to freeze the gas molecules thereby creating vacuum and is able to reach ultra-high vacuum (UHV). Several challenges exist in miniaturizing a cryopump as the power requirement in creating such low temperatures is quite high, and thermal isolation is hard to achieve at such a small scale. The cold surface could also saturate quickly when used at low vacuum, therefore cryopumps are typically only used to pump from high to ultrahigh vacuum. A MEMS vapor-jet pump also known as a diffusion pump has also been demonstrated with an ultimate pressure of 370 Torr [6].

Ion pumps are able to attain UHV levels and could potentially be miniaturized. The ion pump performance is highly correlated with the available surface area — both the creation of ions and removal of the ions by the getter are highly related to the surface area for both components. Reducing the scale of an ion pump would increase the ratio of the surface area to the pump volume. This will allow for better pump performance. In a macro-scale sputter ion pump, the background molecules are ionized by striking plasma; the ions are sputtered onto a getter which then reacts with the gas molecules and deposit them on the chamber walls. This concept of creating a chip-scale pump with an orbitron pump to sputter ions onto a getter had been proposed [7] and chip-scale sputter ion pumps have been created, though it was only able to pump from 18 Torr to 17.4 Torr [8].

The Chip Scale Micro Vacuum Pump (CSVMP) project seeks to use MEMS technology to create low-power micro vacuum pumps that will evacuate a small volume down to high vacuum from atmospheric pressure. The pump is divided into several components separated by function as seen in Figure 1-1: the first stage of the pump

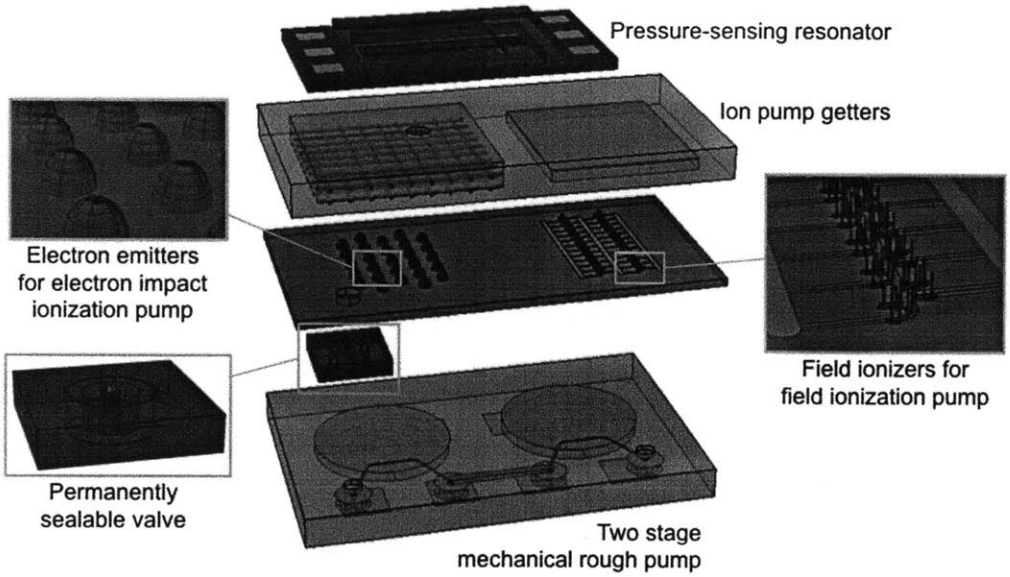

Figure 1-1: A schematic of the Chip Scale Micro Vacuum Pump project. The mechanical rough pump is responsible for pumping down to low-vacuum from atmospheric pressure. The field ionization pump is then responsible down to mid-vacuum level, and the electron impact ionization pump will pump down to the μTorr level.

will be a two-stage mechanical roughing pump to evacuate from atmospheric pressure to about 30 Torr. The field ionization pump (FIP) evacuates from 30 Torr to the mTorr range while the electron impact ionization pump (EIIP) lowers the pressure to μTorr levels. MEMS isolation valve will encapsulate the vacuum and a resonator will be used to measure the pressure. The volume pumped will be approximately $20\,\mathrm{mm}^3$ while the maximum power usage for the pump will be 1 Watt. The entire pump will take up no more than $2\,\mathrm{cm}^3$ of volume, and features MEMS valves to isolate each pumping stage and a resonator to measure the pressure of the chamber. The FIP will bridge the rough vacuum stage and the high vacuum stage, which traditionally required a turbomolecular pump. Demonstrating a FIP that operates at relatively low voltages (in the 1 kV range) has not been possible without a suitable field enhancer to produce the high field strength necessary for FI. CNTs are ideal for MEMS scale FIP implementation as they are conductive, are mechanically robust, and are able to be created in such a high aspect ratio with a sharp tip. MEMS scale ion pumps have not been previously explored in literature, thus this project will attempt to merge

new methods of creating vacuum in this scale.

The micropump can be used in applications such as chemical sensors and mass spectrometer that need low pressure to increase signal-to-noise ratio. The low power specification will allow for sensors to be packaged in a small and portable system.

1.2 Overview of the Ion Pumps

An ion pump can be created at the MEMS scale with slightly different approaches to the macro scale ion pumps. Ions can be created via electron impact ionization (EII) or by field ionization (FI) and the ions can be buried in a getter via ion implantation. In EII electrons are emitted from the tip of the structure due to tunneling when the surface barrier is distorted by the applied electrostatic field. The emitted electrons are accelerated and then collide with the molecules causing them to fragment and ionize. In an EII pump (EIIP) the molecules then are implanted in a biased getter to create vacuum. It is important to note that since the field emitters are biased at a lower potential, the positive ions that are formed will be attracted to the emitters leading to ion bombardment and tip erosion, especially so at low vacuum [9–13]. Using a second biasing gate to repel these back-streaming ions may help protect the emitters in an EIIP, and for this reason EII designs are more complicated [14, 15].

In FI a very high field strips the gas molecules of their electrons to ionize them. In a FI pump (FIP) the positively charged ionized molecules will then be implanted into a getter structure that is biased negatively. Gas molecules are removed from the enclosed space to create vacuum. EII is considered a hard form of ionization whereas FI is considered to be a soft ionization method. Though the EII method will require about an order of magnitude lower electric field strength than field ionization, it produces more fragmented ions [16, 17]. For this reason FI and a similar phenomenon of field desorption (FD) have received a lot of attention in the field of mass spectrometry since the mass of the molecules stay intact. Though popular from the mid-1970s to the 1980s FD and FI eventually gave way to other forms of ionization such as fast-atom bombardment and electrospray ionization for mass spectrometry use [18].

Unique capabilities of using FI for mass spectrometry have been discovered recently in the past decade [19–21]. Several methods of microfabrication exist to create a field ionizer such as using protrusions on a razor blade [22], vertical ZnO nanowires [23], vertically isolated CNTs [24], and whiskered silicon nanowires [25]. The ionizing tip on an FI device does not go through ion bombardment and tip erosion since the ionized molecule with a negative charge is repelled by the positive tip. FI devices therefore should be suitable for higher pressure operation compared to EII sources .

In the CSVMP project the EIIP will pump from mid-vacuum to high-vacuum. The FIP does not need such high vacuum levels to operate and therefore will be used to reach mid-vacuum levels. It will act as the second stage of the pump and will be the focus of this project.

1.3 Thesis Organization

The motivation for this project and a brief overview of the existing pumping technologies were described in Chapter 1. In Chapter 2 the fundamental theory of field emission and field ionization is discussed. Understanding these phenomena and how they relate to the device geometry is crucial in selecting the device architecture and designing the device for optimal performance and ease of fabrication. In Chapter 3 we present the device structures for the FIP we investigated in this thesis. Chapter 4 presents the results from electrostatic simulations and estimation of the FIPs performance. Chapter 5 covers the fabrication of the devices. Chapter 6 analyzes and discusses the electrical characterization done on one of the test devices. Lastly, Chapter 7 summarizes the work done, the results and recommendations for future work including the types of tests needed to verify the pumps operation.

Chapter 2

Background & Theory

2.1 Theory of Field Ionization

In field ionization a strong electric field is applied between the tip and the gate of the device, which causes the potential barrier between the tip and the gas molecules to deform, leading to electrons tunneling from the gas molecules into the tip. The molecules that lost electrons are now ionized, and they are accelerated to a getter that is negatively biased and embedded in the getter.

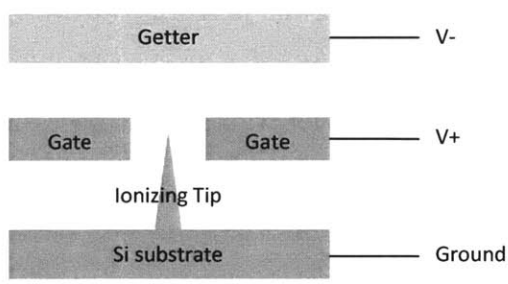

Figure 2-1: A field ionization pump schematic

The field ionization process can simply be put as

$$M \rightarrow M^{+} + e^{-} \tag{2.1}$$

where M represents the gas phase molecule that is ionized.

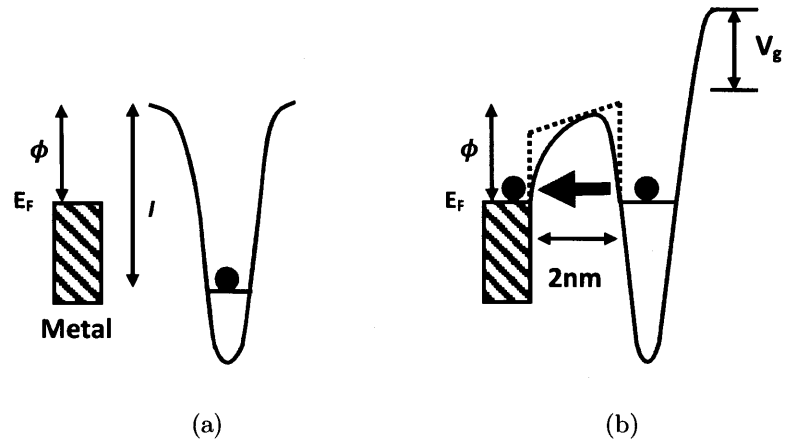

Figure 2-2: Potential well diagram of a molecule going through field ionization: (a) undistorted (b) in a strong field gradient biased by V_g. The valence electron of the molecule is raised to the Fermi level and tunneling may occur. The trapezoidal approximation of the barrier is shown.

Ionization energy I is the minimum energy required to remove an electron from a molecule, and it is analogous to the work function ϕ for metal. This represents the energy required to remove the outermost electron from the molecule. When an electric field is applied to a gas molecule, the potential barrier deforms from its unperturbed state. With a high enough field, the potential barrier will deform and allow electrons to tunnel through the finite barrier width. The process is defined as field ionization. The energy level of the electron in the gas molecules must be elevated above the Fermi level of the tip material for electrons to tunnel into the tip. Figure 2-2 shows how the potential well of a molecule is deformed during field ionization.

Note that CNTs have a work function of about 5 eV [26, 27]. If the molecules are too close to the tip ionization will not occur due to the absence of empty states below the Fermi level [28]. If the tip is too small the tip may burn out due to Joule heating from the high current, and if the tip is too large the tip will not create a sufficiently high field for field ionization.

The simplest case for quantitative analysis is when a sufficiently strong electric

field is applied at the tip that will result in all of the gas molecules near the tip to be ionized. In this strong-field regime the ion current is limited by the amount of un-ionized neutral gas molecules near the tip and hence it is said to be supply-limited. The number of molecules going into this ionization zone is directly proportional to the pressure of the chamber. The ionization current is expressed as

$$I_i = q \cdot \left(\frac{P}{kT}\right) \cdot C_t \cdot A \tag{2.2}$$

where q is the electron charge, P is the pressure, k is Boltzmann's constant, T the temperature in kelvin, C_t is the thermal speed of the molecule, and A is the cross sectional area of the ionization sphere.

Another possibility is the barrier-limited ionization that occurs in the low-field regime. In this case only the gas molecules very close to the tip will have sufficient probability of being ionized. The ion current will depend on the number of molecules near the tip and the lifetime of the molecules (τ). The lifetime depends on the frequency at which the electrons arrives at the potential barrier (f) and the tunneling probability (D) where $\tau = \frac{1}{fD}$. With this, the current for field ionization has been modeled by Gomer [28] to the first-order as

$$I_i = q \cdot \left(\frac{P}{kT}\right) \cdot \nu \cdot f \cdot D \tag{2.3}$$

where ν is the ionization volume, f is the barrier attempt frequency and D expresses the tunneling probability. Gomer uses the expectation value of momentum p_e and effective radius r_e for the s-state orbital to estimate the arrival rate of electrons at the barrier as

$$f = p_e / (2mr_e) \tag{2.4}$$

The barrier attempt frequency f is estimated to be in the order of 10^{15} to 10^{16} sec^{-1} [28, 29]. There is a minimum distance between the ionizing metal surface and the molecule. If the molecule is too close to the surface, ionization would not occur due to the absence of empty states below the Fermi level. This critical distance X_C is

$$X_C = \frac{I - \phi}{F} \tag{2.5}$$

As the distance between the molecule and the tip grows, the barrier width also grows, which decreases the tunneling probability D. The tunneling probability is approximated using the trapezoidal area formed between the metal tip and the molecule using the Wentzel-Kramers-Brillouin (WKB) approximation as

$$\begin{aligned} D_{WKB} &= \exp\left(-2(2m/\hbar^2)^{1/2}\int_0^l (V-E)^{1/2}dx\right) \\ &= \exp\left(-2B\int_0^{X_C}\left(\phi + \frac{I-\phi}{X_C}x\right)^{1/2}dx\right) \\ &= \exp\left(-\frac{B}{F}\cdot\left(I^{3/2} - \phi^{3/2}\right)\right) \end{aligned} \tag{2.6}$$

where m is the electron mass, $\hbar$ is the Dirac constant, V is the potential energy of the electron, E is the kinetic energy, l is the barrier width, $B = 6.8 \cdot 10^7 \left[\mathrm{VeV}^{-3/2}\mathrm{cm}^{-1}\right]$, I is the ionization energy of the gas molecule, ϕ is the work function of the metal tip, F is the applied electric field. The barrier has been approximated as a trapezoid with side heights of I and ϕ as seen in Figure 2-2 [28, 30].

The electric field F can be modeled as

$$F = \beta_{eff} \cdot V_G \tag{2.7}$$

$$\beta_{eff} \propto r^{-1} \tag{2.8}$$

where β_{eff} is the field factor that is dependent on the tip geometry, r is the radius of the tip, and V_G is the voltage applied at the tip. The field factor depends purely on the physical structure of the device. There is a high dependence of the field factor — therefore the electric field — on the tip radius, which makes the high aspect ratio and sharp CNTs a good choice for creating the tip structure.

In order to approximate the field factor that is needed for field ionization, we

assume that the tunneling probability becomes significant when the barrier width is 1 to 2 nm, which is in the order of the de Broglie wavelength of an electron. The barrier width reduces to this size when a field strength of the order of $1 \cdot 10^8$ V/cm is applied to the metal surface [31]. Gomer was the first to observe that a field strength of about 10^8 V/cm was needed to field ionize hydrogen molecules [28]. Hydrogen (H_2) has an ionization potential of 15.43 eV which is close to the ionization potential of the atmospheric gasses such as oxygen (O_2), nitrogen (N_2), argon (Ar) and carbon dioxide (CO_2) at 12.08 eV, 15.58 eV, 15.76 eV and 13.79 eV respectively. In this thesis $1 \cdot 10^8$ V/cm will be used in estimating the ionization volume where the gas molecules will tunnel with probability D.

2.2 Comparison to Electron Impact Ionization and Field Emission

Electron impact ionization is a form of ionization where energetic electrons collide with molecules to ionize them. This ionization can be represented as

$$M + e^- \rightarrow M^+ + 2e^- \tag{2.9}$$

where M represents the neutral gas phase molecule that will be ionized. Both M^+ cations and M^- anions are produced, though the ratio of cations to anions ranges from $10^2 : 1$ to $10^4 : 1$ because cation formation from a neutral molecule by electron impact is a much more efficient process than an anion formation by electron capture [31, 32]. Electron impact ionization therefore can be seen as a two-step process where the first step is the creation of electrons to be used in the reaction and the second step of accelerating those electrons to the molecules to ionize them.

Figure 2-3 shows the potential diagram of the field emission phenomenon.

The Fowler-Nordheim (FN) equation describes the current density due to field emission. As a function of the bias voltage, the current is described as

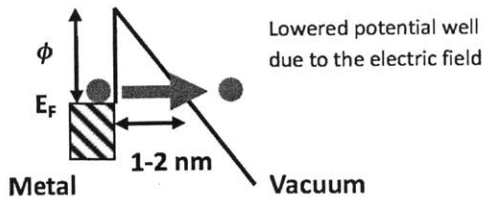

Figure 2-3: Potential well diagram of an electron during field emission

$$I = \alpha_{FN} V^2 e^{-b_{FN}/V} \tag{2.10}$$

where

$$\alpha_{FN} = \frac{\alpha A \beta^2}{1.1\phi} \exp\frac{B\left(1.44 \cdot 10^{-7}\right)}{\phi^{1/2}} \qquad b_{FN} = \frac{0.95 B \phi^{3/2}}{\beta}$$

and $A = 1.54 \cdot 10^{-6}\,\mathrm{AV^{-2}eV^{-1}}$ and $B = 6.87 \cdot 10^{7}\,\mathrm{VeV^{-3/2}cm^{-1}}$. α is the effective emitter area, ϕ the workfunction and β is the field factor.

Equation 2.10 can be rearranged to

$$\ln\left(I/V^2\right) = \ln\left(\alpha_{FN}\right) - \frac{b_{FN}}{V} \tag{2.11}$$

which shows that $\ln\left(I/V^2\right)$ varies linearly with $1/V$ by a factor of b_{FN}, from which β can be extracted.

In the EII process, the field emitted electrons are accelerated above the ionization potential of the gas molecules. Only some of these electrons are able to ionize the neutral molecules. The ratio of the ion current to the emitted electron current is defined as the ionization efficiency, and is described as

$$\frac{I_I(E)}{I_E(E)} = \rho \cdot L \cdot \sigma_{Total}(E) \tag{2.12}$$

where $I_I(E)$ is the ion current, $I_E(E)$ is the electron current, ρ is the molecule density in the chamber, L is the collision pathlength, and $\sigma(E)$ is the total ionization cross section, which is a measure of the probability that a given ionization process will occur when a molecule interacts with an electron. To eject the outermost electron of a molecule, the field emitted electron must have higher energy the ionization potential

of the outermost electron. The total ionization cross section increases as the electron energy increases, and is maximized when the electron has the same energy as the outermost orbiting electron. Any further increase in energy decreases the ionization cross section due to the shortened interaction time between the electron and electrons of the gas molecule [33].

Chapter 3

Device Structure and Architecture

Two broad design architectures were explored in this project. The second architecture was created to improve on the first. Arrays of carbon nanotube (CNT)-based devices were used in both.

Ever since CNTs were first reported in 1991 [34], their extraordinary mechanical, electrical and thermal properties have made them a topic of interest for many research applications [35–37], in particular in field emitter arrays (FEAs) [38–42]. CNTs are chemically and mechanically robust, and are well suited for device fabrication processes that require high temperature steps after the CNT growth. CNTs high aspect ratio and sharp tips provide the high field factor needed for high electric field strength and therefore field ionization.

The initial device architecture used a horse-shoe shaped design, where the gate and tips were both comprised of CNTs. Surrounding and equidistant from the ionizing tip CNT would be the gate CNTs used to bias the tip CNT. This design exhibits a highly transparent ionizing tip allowing for higher chances of ion creation. The surrounding gate structures are also created with CNTs. After fabrication issues were discovered with this approach, the design was modified into a design with a layer-by-layer approach that resembles a floral shape — a central high-field aperture surrounded by neutral flux apertures — and another that uses a self-aligned gate method of defining the gate aperture. This layered approach allows for more consistency during the fabrication process and exhibits a higher field factor compared to the horse-shoe design.

Both approaches are detailed in the following sections.

3.1 Horse-shoe (co-planar) Design

The proposed design called for vertically aligned CNTs to make up the gate and the tip portion of the device. The gate CNTs would all have the same potential while the tip would be set to a different potential to create the electric field. Using CNTs for the gate structure allows the gas molecules to reach the tip to be ionized with high transparency, which increases the flux of neutral molecules to the ionization region. The proposed design is shown in Figure 3-1.

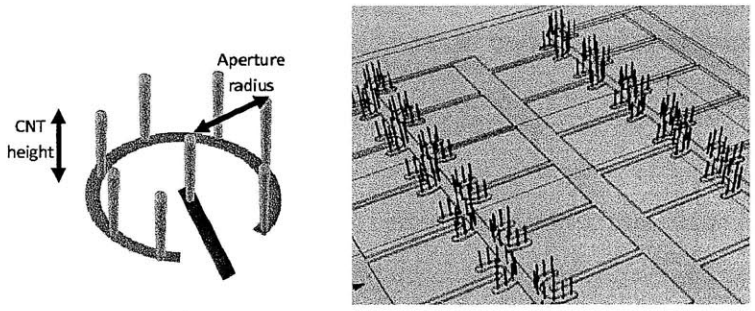

(a) (b)

Figure 3-1: The original horse-shoe design of one field ionization pump. The tip and the gate structures are all comprised of CNTs. (a) A single pump structure (b) arrangement of the array

The distance between the tip and the gate is 2 μm for half of the devices, and the other half 3 μm, as seen in the mask layout in Appendix A.

3.2 Floral (layer-by-layer) Design

The second design for the FIP allows for a simplified and more reliable fabrication process. The main structural difference compared to the original design is that the silicon substrate acts as one of the electrodes and is electrically connected to the ionizing CNT tip. The tips are arranged in a hexagonal array with 5 μm pitch to

allow sufficient separation between each unit. The gate structure is not comprised of several CNTs but rather a flat layer of n-type amorphous silicon (n-a-Si), which is electrically isolated from the substrate by a layer of oxide. This gate structure resides in the same plane as the ionizing tip and has an aperture opening in which the tip is centered. The floral shape comes from additional holes made on the gate to allow gas molecules to gain greater access to the ionizing tip. The aperture radius is $0.4\,\mu$m to maximize the field factor.

Note that as the device specification requires the use of voltages of up to 1 kV, a minimum thickness of oxide will be needed between the substrate and the gate electrode. Assuming a maximum dielectric field strength of $300\,\mathrm{V}/\mu\mathrm{m}$ for PECVD oxide, around $3\,\mu$m oxide will be needed to separate the two conductive layers. This also necessitates the CNTs height to be at least $3\,\mu$m.

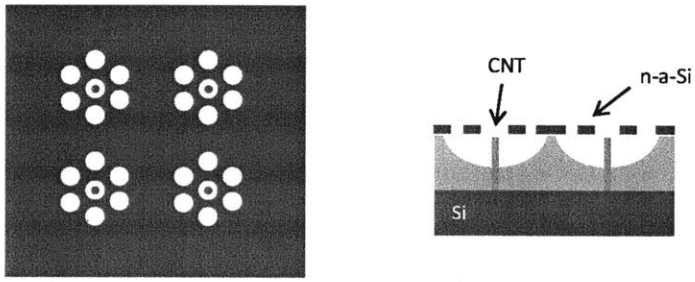

(a) (b)

Figure 3-2: Diagram of the floral device array: (a) top view (b) cross-sectional view

3.3 Self-aligned-gate Design

An even more simplified design using self-aligned fabrication methods was explored in addition to the floral shape design. This self-aligned-gate design would eliminate the need to use photolithography to define the gate aperture, a process that requires the utmost precision and can be inconsistent between different device wafers. The layer-by-layer approach is still preserved and a layer of oxide separates the two conducting

layers. The aperture radius is determined by the amount of oxide deposition, and therefore is increased to approximately 1 μm.

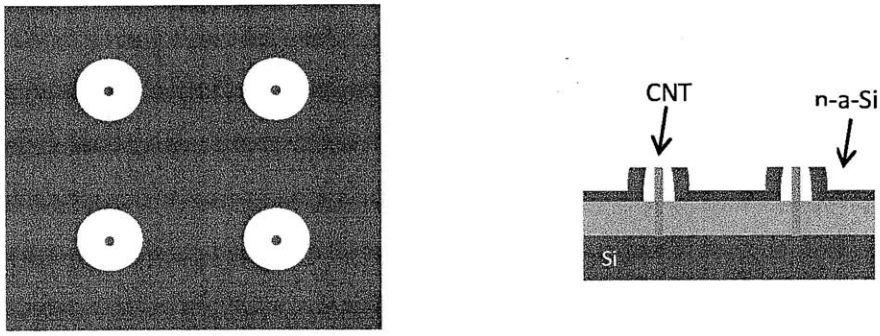

(a) (b)

Figure 3-3: Diagram of the self-aligned-gate device array: (a) top view (b) cross-sectional view

Chapter 4

Device Modeling

As stated in Equation 2.3, the ionization current in field ionization in the low-field limit can be modeled to first order as

$$I_i = q \cdot \left(\frac{P}{kT}\right) \cdot \nu \cdot f \cdot D$$

We need to estimate the ionization volume (ν), the barrier attempt frequency (f) and the tunneling probability (D), and assume a pump volume and leak rate to forecast the pump performance.

4.1 FEM Electrostatic Simulation

In order to estimate the ionization volume, the devices were modeled using electrostatic Finite Element Method (FEM) simulations via COMSOL and Ansoft Maxwell SV. FEM simulations are useful for electrostatic calculations as they are able to handle complex geometries and boundaries while reaching accurate results through convergence. A result of such simulation using Maxwell is seen in Figure 4-1.

The dependence of field factor on the various parameters such as the radius of the tip, distance between the gate and the tip, height of the CNTs was analyzed to find the field factor that is characteristic of the design.

Simulations were first run for the horse-shoe design. $1\,\mu$m tall CNTs with 40 nm tip radii and $1\,\mu$m distance between the tip and the gate produced a field factor (β) of $1.5 \cdot 10^5\,\mathrm{cm}^{-1}$ 20 nm from the surface of the tip. In this case, since $F = V_G \cdot \beta$, less than 700 V would be needed to be applied to the tip in order to achieve a field strength of $1 \cdot 10^8\,\mathrm{V/cm}$ required for field ionization. The voltage required for field ionization is shown to be heavily dependent on tip radius and to a lesser degree on other geometric factors (such as height of the CNTs and gate aperture radius), which will vary within the array due to variations exhibited during the fabrication process. This initial simulation run showed that the horse-shoe design would yield a feasible FIP.

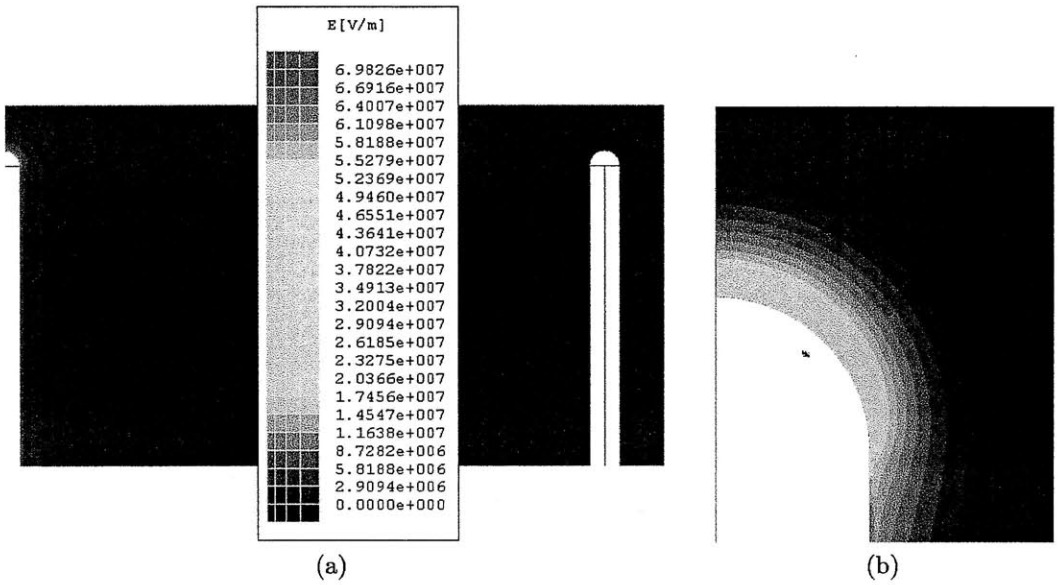

Figure 4-1: Axisymmetric Maxwell SV Simulation of a CNT tip with a 30 nm radius with $2\,\mu$m aperture radius at 1 V andfor the horse-shoe design: (a) the entire test setup (b) close-up of the tip

For the updated floral and self-aligned gate designs a more exhaustive modeling was done to characterize the field strength and its dependence on the distance from the tip as well as the tip radius. The two designs share similar features and geometries for the gate and the tip that both simulations were done together. The most noteworthy difference in design compared to the horse-shoe design is the reduced aperture radius of less than a micron and the increased height of the CNTs to $3\,\mu$m. Figure 4-2 shows

a simulation run done for a 40 nm radius tip with a 0.4 μm aperture radius.

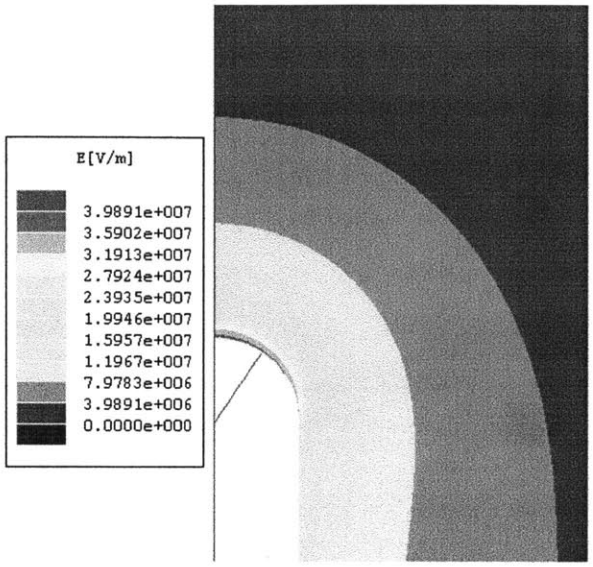

Figure 4-2: Axisymmetric Maxwell SV Simulation of a CNT tip with a 20 nm radius and 0.4 μm aperture radius at 1 V

The red line originating from the middle of the tip shows the direction along which the electric field was measured. The simulations were run with tip height of 2 μm, gate aperture radius of 0.4 μm for various tip radii. Summary of the field strength dependence on distance and tip radius are shown below in Figure 4-3.

The highest field strength was achieved with the smallest tip radius of 20 nm. To approximate Gomers field factor in Equation 2.8, $1/r$ is also plotted, which is closely matched by the maximum field strength calculated using FEM.

To simplify the estimation of the ionization volume, low-field regime for field ionization was defined as any area above $1 \cdot 10^8$ V/cm. The ionization volume for one ionizing tip was estimated to be the volume of half of a sphere with radius at which field ionization can be achieved with 1000 V bias voltage less the tip volume.

$$\nu = \frac{1}{2} \cdot \frac{4}{3} \cdot \pi \cdot \left(r^3_{low_field_regime} - r^3_{tip} \right) \tag{4.1}$$

Though the 20 nm tip was able to achieve higher electric field strength using the same bias voltage, the field strength diminished too quickly for its ionization volume

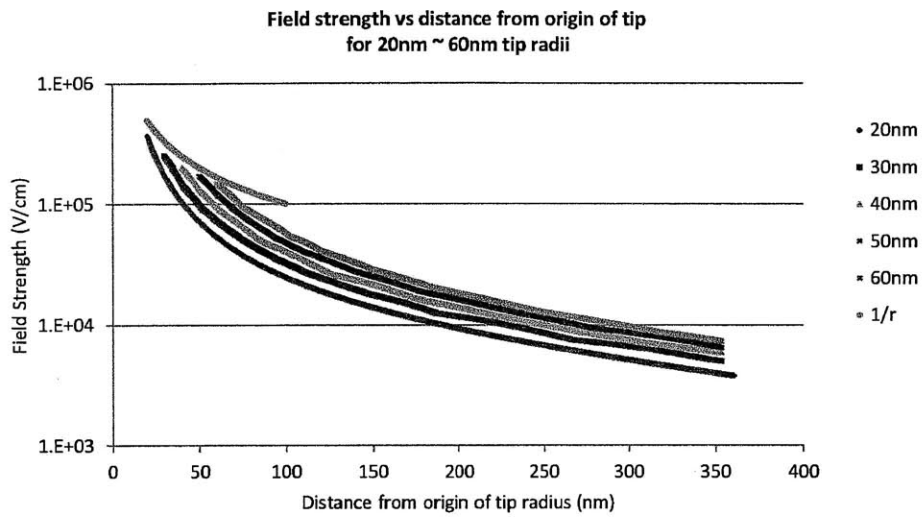

Figure 4-3: Field strength dependence on distance from the tip for various tip radii. The tip is biased at 1 V and the gate aperture radius is 0.4 μm. The distance is measured from the origin of the tip radius. Note that there is no electric field inside the conducting tip.

to be the highest. Summary of the ionization volumes compared to tip radius can be seen in Figure 4-4.

4.2 Estimation of the Tunneling Probability

The calculation of the tunneling probability (D) is quite complex due to the nature of the wave equation. WKB approximations are used to find an estimate. The analytical approximations of the tunneling probability was described in Equation 2.6, and is as follows:

$$D_{WKB} = \exp\left(-\frac{B}{F} \cdot \left(I^{3/2} - \phi^{3/2}\right)\right)$$

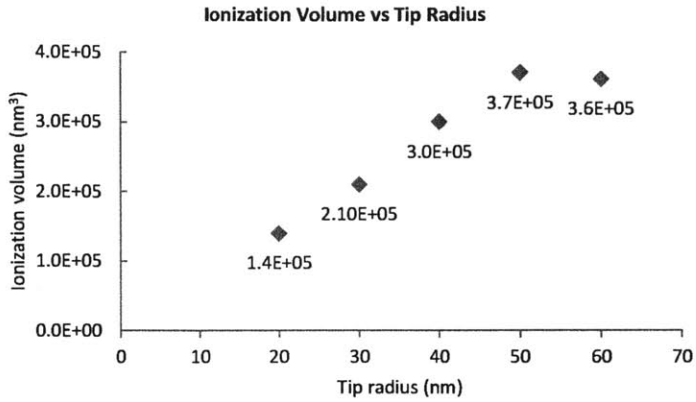

Figure 4-4: The ionization volume for various tip radii at 1000 V tip bias

where B is a constant of $6.8 \cdot 10^7$ $\mathrm{VeV}^{-3/2}\mathrm{cm}^{-1/2}$, I is the ionization energy of the molecule in eV, ϕ is the work function of the cathode in eV, and $\beta \cdot V_g$ the electric field strength in V/cm. As mentioned in Chapter 2, CNTs work function is around 5 eV, and the ionization energy of N_2 is 15.58 eV, O_2 is 12.08 and Ar is 15.76 eV.

Using Equation 2.6 the tunneling probability for different atmospheric gases are calculated for field strength of $2 \cdot 10^8$ V/cm, which is attainable with 1000 V bias and 40 nm tip radius: for N_2 the tunneling probability is $1.11 \cdot 10^{-7}$, for O_2 $3.17 \cdot 10^{-5}$ and for Ar $8.24 \cdot 10^{-8}$. As N_2 is the most abundant atmospheric gas by far, $D = 1 \cdot 10^{-7}$ will be used for the purposes of estimating the pump performance with bias of 1000 V for 40 nm tip radius structures.

4.3 Comparison to Previous Work

Data from previous work was compared to our model to estimate the performance we could expect from our device and gauge the accuracy of our model. Field ionization arrays were previously tested by Chen, where her field emitter array was tested in field ionization mode in two different pressures of Ar [24]. The data for the ionization current has a low magnitude and with a wide spread, so four data points were

Tip Voltage	500 V	570 V
P (Torr)	I (Amps)	I (Amps)
8.5e-4	3e-12	1.0 e-11
5.6e-3	1.5e-11	1.5e-10

Table 4.1: Extracted data from Chen's field ionization tests

extracted at the extremes and are summarized in the following table.

Our previously estimated electrical characteristics can be compared to this data to validate our model. Note that for any given bias voltage — and therefore a fixed ionization volume — the ionization current should be directly proportional to the pressure, though this is not the case in this experimental data. The ratio of pressures is 6.6, though the ratio of the currents is 5 with 500 V bias and 15 with 570 V bias. Although this shows some intrinsic limitation of fitting this experimental data to our modeling, this comparison will be used to coarsely validate our model.

The ionization volume was derived from Chen's estimate of her tip radius at 20 nm and matching it to our simulation results on the ionization volume. A conservative estimate of $10^{15}\,\mathrm{sec}^{-1}$ is used for the barrier attempt frequency. Tunneling probability is calculated for Ar, the gas used for her experiment. The field factor, which is solely based on the device geometry, is taken from her experimental data and is around $5 \cdot 10^5\,\mathrm{cm}^{-1}$ for the 10x10 arrays used in her test. From this, the field strength at the CNT-vacuum boundary is calculated for the two different biases used in the experiments, which is then used to calculate the tunneling property using Equation 2.6.

The array size is estimated by assuming a yield of 30% on her 10x10 size array used for the field ionization test. Using these parameters and our best assumptions of Chen's devices we estimate the ionization current her devices would exhibit using our model.

In estimating how Chen's device would perform, the parameters in Table 4.2 were used. After estimating the values that Chen's device would have exhibited, comparison was done to her experimental ionization current data, which is shown in Table 4.3.

	500 V	570 V	Assumptions
Ionization volume per tip (ν)	$2.8 \cdot 10^{-17}\,\mathrm{cm}^3$	$4.0 \cdot 10^{-17}\,\mathrm{cm}^3$	$r = 20\,\mathrm{nm}$
Tunneling probability (D)	$8.0 \cdot 10^{-6}$	$3.4 \cdot 10^{-5}$	$\beta = 5 \cdot 10^5 cm^{-1}$
Barrier attempt frequency (f)	$10^{15}\,\mathrm{sec}^{-1}$		
Array size	30		30% yield

Table 4.2: Parameters used in estimating Chen's device performance for field ionization

Estimation of Chen's device performance		
Bias	500 V	570 V
P (Torr)	I (Amps)	I (Amps)
8.4e-4	2.9e-11	1.2e-10
5.6e-3	1.9e-10	8.1e-10

Chen's data	
500 V	570 V
I (Amps)	I (Amps)
3.0e-12	1.0e-11
1.5e-11	1.5e-10

Table 4.3: Comparison of Chen's device performance estimation and experimental data

Our calculation overestimated Chens device performance by a factor of 5.4 to 12.7, within an acceptable range of error. This difference can be attributed to our conservative estimation of the ionization volume and barrier attempt frequency, the number of working devices in Chens device array, and the estimation of the tunneling probability.

To better understand the variation between our model and Chens experimental data and gain insight into our models dependence on individual parameters, a sensitivity analysis was done for each of the non-linear variables. The full analysis is shown in Appendix C, and the summary is shown below:

For all of our models we assume the average gas temperature to be 300 K. This can vary due to the heating of the ionizing tips which may raise the gas temperature, or lower due to pumping of the chamber. The ionization current is inversely proportional to the temperature.

The ionization volume can vary due to the variation of the CNT tip radius. As seen in Figure 4-4 the variation of the tip radius had a limited effect on the ionization volume. The sensitivity analysis for radius was done for the 20 nm, 30 nm, and 40 nm tips with bias of 500 V.

Our model is directly proportional to the barrier attempt frequency f, which may

Variable	Varied parameter	Baseline Parameters	Amount of variation	Ratio to baseline
$1/T$	T		$\pm 10\%$	$0.91 \sim 1.11$
			$\pm 50\%$	$0.67 \sim 1.5$
ν	r_{tip}	$r_{tip} = 20\,\mathrm{nm}$ $V_g = 500\,\mathrm{V}$	$+50\%$	2.50
			$+100\%$	4.29
D	β	$\beta = 5 \cdot 10^5\,\mathrm{cm}^{-1}$ $V_g = 500\,\mathrm{V}$ $\phi_{CNT} = 5$ eV	$\pm 10\%$	$0.21 \sim 3.61$
			$\pm 50\%$	7.4 E-7 $\sim$ 110
D	ϕ_{CNT}	$\phi_{CNT} = 5$ eV $\beta = 5 \cdot 10^5\,\mathrm{cm}^{-1}$ $V_G = 500$ V	$\pm 10\%$	$0.63 \sim 1.60$

Table 4.4: Sentivity analysis of the non-linear variables in the model

be underestimated by as much as a factor of 10. A more thorough analysis of f is omitted from this thesis due to its complexity depending on the gas element and orbital of the outer most electron.

Our model for the ionization current is highly sensitive to the tunneling probability D, which is somewhat sensitive to the CNT work function ϕ_{CNT} and highly sensitive to the field factor β. This is as expected due to the exponential relationship that the work function and field factor have on the tunneling probability as seen in Equation 2.6. Chen's experimental data — which had a deviation factor of 12.7 from the model — is within the error bounds of this analysis using the lowest amount of variation ($\pm 10\%$, except $+50\%$ for radius) which yields a deviation factor of 16. For a more accurate model, an accurate estimate of the field strength near the ionizing tip as well as the work function of the CNT is needed.

4.4 Pump Performance Calculations

In order to model the pump performance, we assumed that all of the ionized molecules are implanted into the getter and there is neither charge recombination nor neutralization. The ionization current is directly proportional to the chamber pressure, as stated in Equation 2.3, which means that the pump rate is directly proportional to the chamber pressure.

$$\frac{dP}{dt} = \left(\frac{dN}{dt} \cdot k_b \cdot T\right)\Bigg|_{\substack{constant \\ volume}} \tag{4.2}$$

$$\frac{dN}{dt} = \dot{N}_{out} = -c_1 \cdot N \tag{4.3}$$

$$c_1 = \frac{\nu}{V} \cdot f \cdot D$$

where N is the number of molecules in the chamber, ν is the ionization volume, V is the chamber volume. From here we add the effects of leakage, which can be estimated as

$$\dot{N}_{lk} = \frac{Q \cdot P_{atm} + O_r \cdot A_s}{kT} \tag{4.4}$$

where $\dot{N}_{lk}$ represents the leakage rate in molecules per second, Q is the leak rate at standard conditions, O_r is the outgassing rate and A_s is the surface area of the chamber. Leakage will result from the chamber ports and valves. Outgassing will primarily result from desorption from the chamber walls and bulk. Combining the pumping and leakage rate we get

$$\frac{dN}{dt} = \dot{N}_{out} + \dot{N}_{in} = -c_1 \cdot N + \dot{N}_{lk} \tag{4.5}$$

Solving the differential equation, we get

$$N(t) = \left(N_o - \frac{\dot{N}_{lk}}{c_1}\right) \cdot e^{-c_1 t} + \frac{\dot{N}_{lk}}{c_1} \tag{4.6}$$

$$N_{t\to\infty} = \frac{\dot{N}_{lk}}{c_1} = \dot{N}_{lk} \cdot \frac{V}{\nu} \cdot \frac{1}{f \cdot D} \tag{4.7}$$

In order to reduce the terminal pressure of the pump, the leak rate must be minimized and the ionization volume maximized.

Pump performance was estimated using MATLAB. The following assumptions were made:

Chamber volume	$20\,\mathrm{mm}^3$
Initial pressure	30 Torr
Ionizing tip bias	1 kV
Ionizing tip radius	40 nm
Pump array size	50,000 field ionizers
Barrier attempt frequency	$10^{15}\,\mathrm{sec}^{-1}$
Tunneling probability	10^{-7}

The chamber volume was chosen as a volume that a chip scale vacuum pump would be expected to pump. Tip radius of 40 nm is chosen, which is the radius exhibited by most of our CNTs. The barrier attempt frequency is a conservative estimate, and the tunneling probability assumes a field strength of $2 \cdot 10^8$ V/cm, attained at the surface of the 40 nm radius tip with 1000 V bias. An array size of 50,000 is equivalent to an array area of $1\,\mathrm{mm}^2$ with $5\,\mu$m pitch between the ionizers. The ionizing tip bias voltage and tip radius were used to determine the ionization volume per tip, which is calculated to be $3.7 \cdot 10^{-16}\,\mathrm{cm}^3$. The result of pumping performance calculation is seen in Figure 4-5. The leak rate should remain between $1 \cdot 10^{-8}\,\mathrm{cm}^3$ and $1 \cdot 10^{-9}\,\mathrm{cm}^3$ in order to reach mTorr level using a FIP with array size of 50,000.

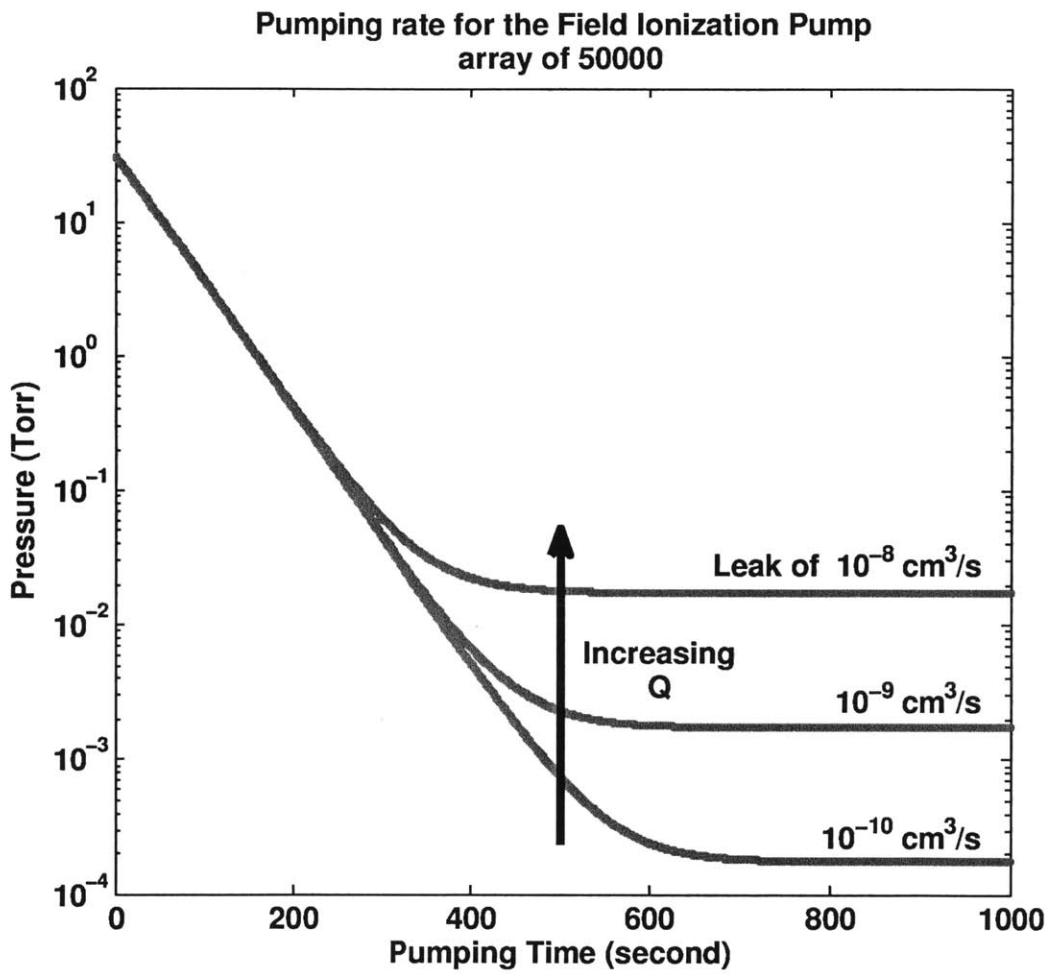

Figure 4-5: MATLAB calculation of pump performance with various leak rates

Chapter 5

Device Fabrication

5.1 Horse-shoe (co-planar) Device Fabrication

The devices were fabricated in MITs Microsystems Technology Laboratory (MTL).

A summary of the process steps for the horse-shoe device is shown below in Figure 5-1. We start with an n-Si wafer and the standard photolithography methods are used to pattern the alignment marks, which is then plasma etched. The alignment marks will aid in aligning the Ni catalyst nanodot patterns onto the horse-shoe looking TiN layer. After the alignment marks are etched, the photoresist is ashed, and the wafer goes through a RCA clean. 3 μm of oxide and 50 nm of amorphous silicon (a-Si) are deposited onto the wafer. The oxide isolates the substrate from the conductive TiN layer. The a-Si layer was an attempt at curbing the arcing problem during the PECVD step for CNT growth by shielding the oxide layer. Standard photolithography steps are used to pattern the grooves so that the TiN layer can be anchored to the oxide beneath. The a-Si is plasma etched until the oxide is exposed and the photoresist is ashed away. A SEM image of the device at this stage is seen in Figure 5-2.

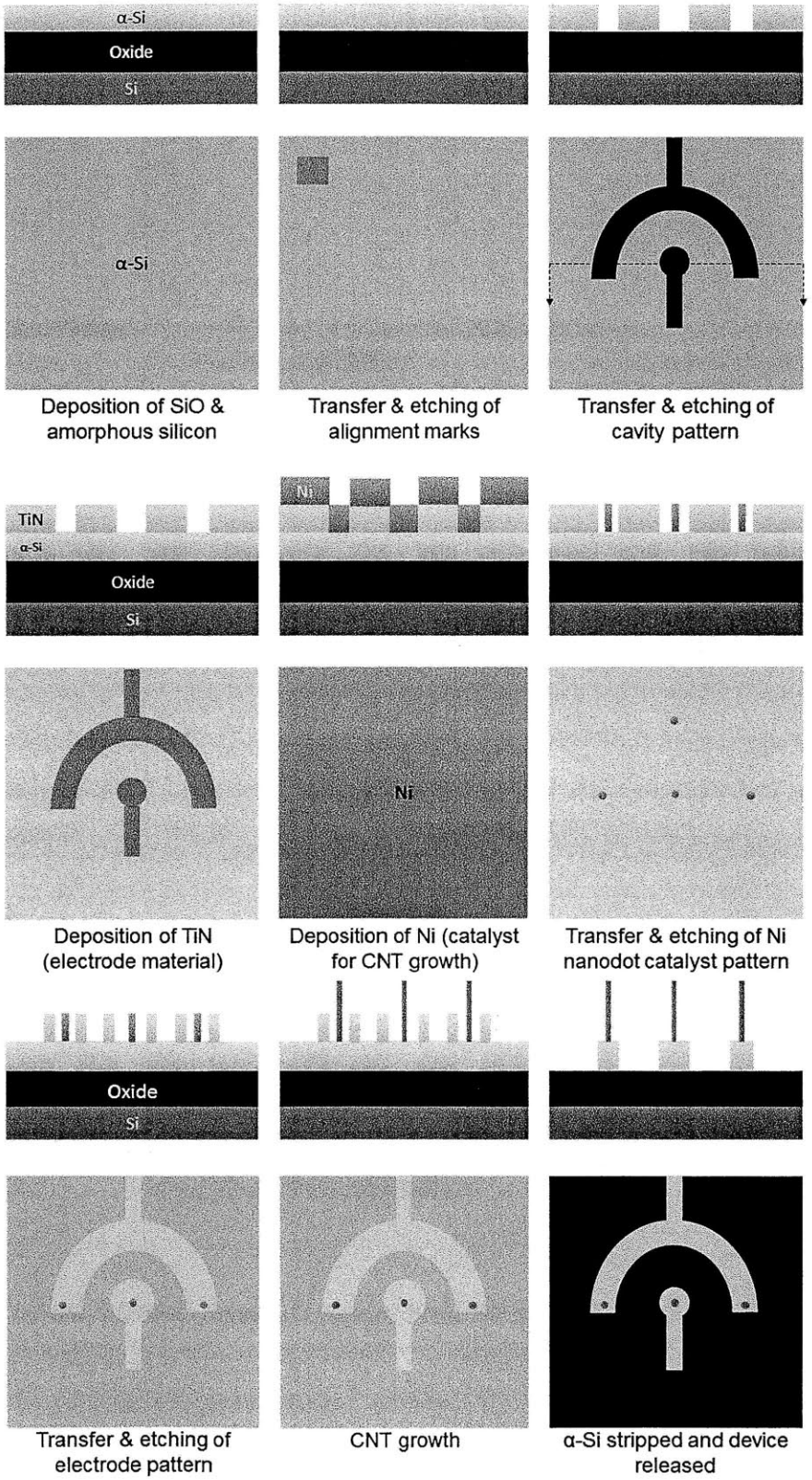

Figure 5-1: Summarized fabrication steps for the original horse-shoe design

The wafer at this point goes through a pre-metal clean, and 50 nm of TiN is sputtered via physical vapor deposition (PVD) and 20 nm of Ni is deposited through e-beam evaporation. The TiN layer is the conductive layer that the test setup probe will contact in order to establish the tip and gate potentials. Ni acts as the catalyst for the CNT growth step.

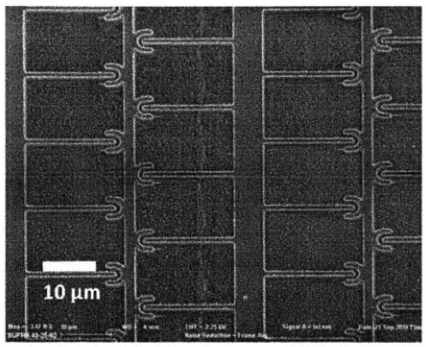

Figure 5-2: The device after the grooves are etched on the a-Si layer

The Ni nanodots are patterned using standard photolithography. These nanodots have a diameter of 0.6 μm. The Ni layer is then wet etched using Transene Ni etchant. This step introduces the most amount of variability in the entire fabrication steps as over-etching could result in no CNTs growing, while under-etching will result in too many CNTs growing from each of the isolated Ni nanodots. The wet-etch is done in an ultrasonic bath which controls the temperature of the bath and can aid in the etch process with the ultrasonic mixing. It was found that the etch rate varied significantly depending on the temperature. The temperature of the bath is set at 27 °C and the ultrasonic level is set at 7 out of 10. Another metric is introduced to establish the correct amount of wet etching. After between 4 to 6 minutes of etching in this condition it is seen that the device wafer goes through a color change as the Ni layer is removed. The TiN layer underneath has a brilliant gold color as the Ni layer is almost completely depleted. This color change transition takes around 7 seconds. The wafer is left to continue to etch 5 more seconds after the color change has subsided, after which it is promptly rinsed with DI water. The photoresist is

ashed. A SEM image of the wafer at this point is seen in Figure 5-3.

With much of the TiN exposed, the electrical layer is then patterned. This layer looks very similar to the grooves made earlier in the n-a-Si layer, only slightly larger to cover the exposed oxide before the CNT PECVD step. Using standard photolithography steps again, the TiN layer is patterned and plasma etched until the a-Si layer is exposed. After the photoresist is ashed the wafer goes through CNT deposition.

The PECVD step for the CNT growth is done at 750 °C for 15 minutes to achieve around 2 μm of height for the CNTs. At this point the device resembles that of the final device. The a-Si layer is then etched away with XeF_2 and the device is released and ready to be tested. SEM images of the device at this step can be seen in Figure 5-4.

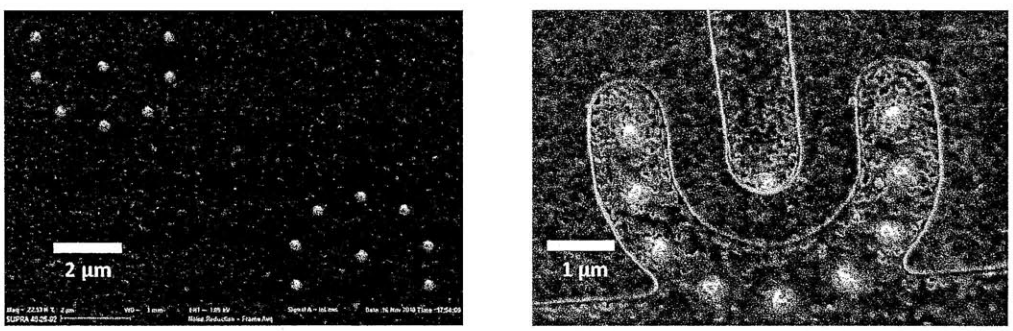

(a) (b)

Figure 5-3: Ni nanodots after patterning and etching. The left picture is of a test wafer that only shows the Ni nanodots while in the right the groove made in the a-Si layer can also be seen.

It is important to note that the a-Si was not able to consistently shield the oxide layer from being exposed to the PECVD process for CNT growth. The result is that arcing occurs that would char the surface of the devices and render them useless. Optical microscope images of the resulting devices are seen in Figure 5-5. Many avenues of fixing the problem was explored such as pulsing the plasma of the PECVD to varying the height of the a-Si providing a conducting path to the a-Si layer to ground in the CNT reactor. As not all devices were charred due to the arcing, some were usable, though the integrity of the oxide layer was often compromised due to

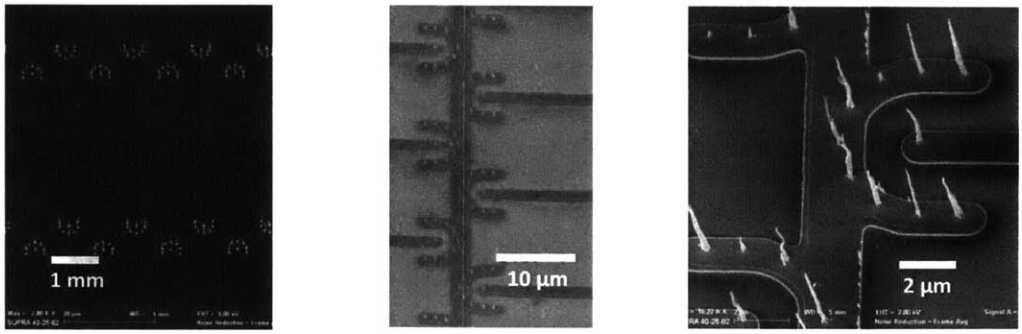

(a) (b) (c)

Figure 5-4: (a) CNTs are seen on a test wafer with no TiN or n-a-Si layer. (b) a device layer with CNTs grown on the TiN layer. The horse-shoe design is clearly seen. (c) Close-up of a device with taller CNTs

the arcing. Though a few devices were completed and even made it to the electrical testing phase, the problems associated with the fabrication of the device resulted in subsequent exploration of a new design to improve the fabrication steps, obtain more robust and fail-proof devices as well as improving the performance of the pumps.

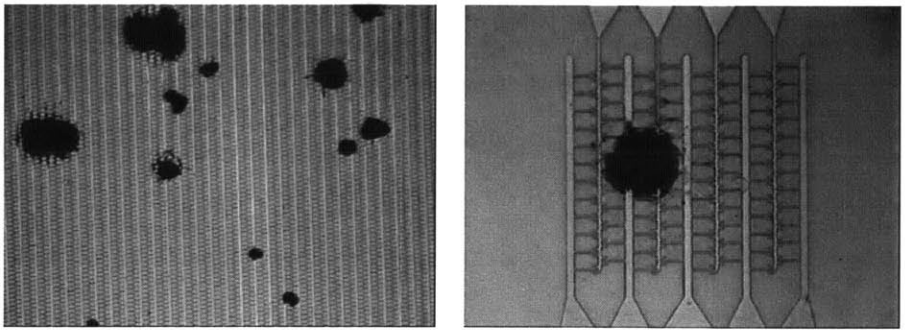

Figure 5-5: The result of arcing due to exposed oxide layer in the PECVD process for CNT growth

5.2 Floral (layer-by-layer) Device Fabrication

The arcing issue seen in the previous designs fabrication was eliminated in a new design scheme that requires no oxide layer to be deposited before the CNT growth. The CNTs are electrically connected to the Si substrate itself, which now acts as one of the two electrodes to bias the ionizing tip.

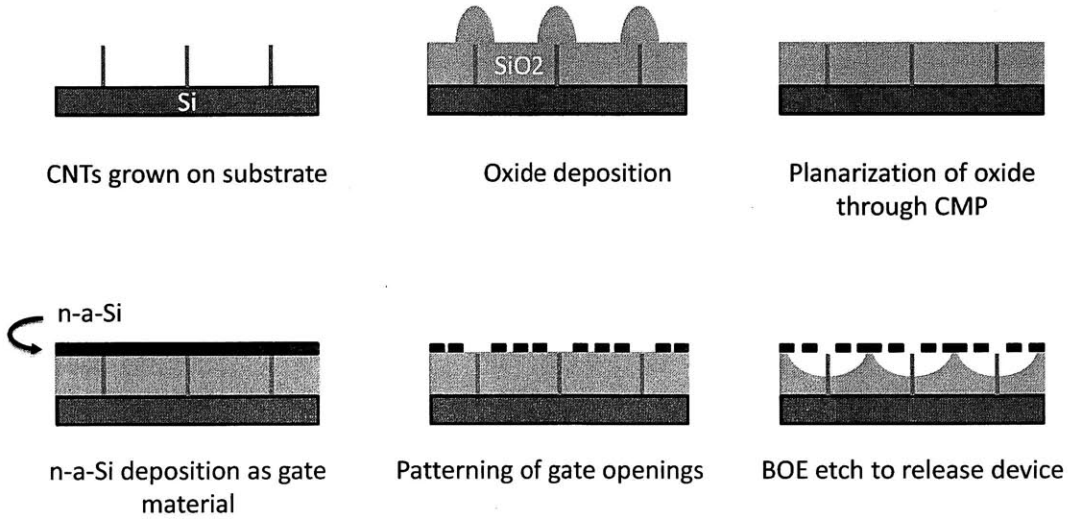

Figure 5-6: Summarized fabrication steps for the floral-design device. Note that the CNTs are positioned on top of TiN pads omitted in the figure. The pads act as a diffusion barrier between Ni and the substrate.

The fabrication steps for this device are summarized in Figure 5-6. To create this device we start off with a blank n-Si wafer. Standard photolithography is used to pattern the alignment marks, which will later aid in aligning the aperture holes on top of the CNTs as well as patterning the gate for device definition. The alignment mark is plasma etched for 180 seconds. After the photoresist is ashed the wafer is Piranha cleaned to prepare for TiN and Ni deposition. 50nm of TiN is sputtered via PVD. This layer will act as the diffusion barrier to the Ni layer and will aid in the CNTs gaining a solid physical and electrical connection to the substrate. The TiN layer undergoes rapid thermal anneal (RTA) at 800 °C for 30 seconds in order to lower resistivity, and increase film density. [43] After this step the TiN layer changes its color from dark gold to bright gold, which improves the visual cues needed during the Ni wet etching step. After the anneal step, 20 nm of Ni is deposited through ebeam evaporation. Ni is used as a catalyst for the tip-growth mechanism through which CNTs are grown. Standard photolithography is used to pattern the Ni nanodots. These nanodots have a diameter of 0.6 μm. The Ni layer is then wet etched using Transene Ni etchant. This step introduces the most amount of variability in the fabrication steps as over-etching could result in no CNTs growing, while under-etching will result in too many CNTs

growing from each of the isolated Ni nanodots. The wet-etch is done in an ultrasonic bath which controls the temperature of the bath and can aid in the etch process with the ultrasonic mixing. It was found that the etch rate varied significantly depending on the temperature. The temperature of the bath is set at 27 °C and the ultrasonic level is set at 7 out of 10. Another metric is introduced to set the correct amount of wet etching. After between 4 to 6 minutes of this etching step, the device wafer goes through a color change as the Ni layer is removed. The TiN layer underneath has a brilliant gold color as the Ni layer is almost completely depleted. This color change transition takes around 7 seconds. The wafer is left to continue to etch 5 more seconds after the color change has subsided, after which it is promptly rinsed with DI water. Prior to using this color change as a feedback mechanism to understand how much etching has been done, the results from this wet etch varied significantly between wafers. This may be due to (1) non-uniform deposition of Ni, (2) different levels of oxidation of Ni due to exposure to the atmospheric gases during fabrication and (3) the condition of the Ni etchant. Using this feedback the variance is controlled somewhat.

After the Ni etch step, the photoresist is kept in place and the TiN layer undergoes plasma etching so that the TiN around the Ni nanodot is etched. This aids in the CNTs growing at the precise location defined by the nanodot mask pattern since the Ni catalyst may move during the early CNT growth processonce the nanodots are annealed they are formed into a sphere due to the surface tension, and in this state the nanodots are more prone to shifting. A SEM image of a few pump sites after this process is shown in Figure 5-7 shown below. After the photoresist is ashed away the Ni catalyst on the TiN pad can be seen as well.

The CNT deposition tool anneals the wafer in order for the catalyst to form a spherical ball. PECVD growth of CNTs is done with the decomposition of acetylene (C_2H_2) at 770 °C for 20 minutes. The CNTs are grown to 3 μm for this design in order to avoid dielectric breakdown between the gate layer and the substrate. The device at this stage can be seen in Figure 5-8.

The CNTs are then covered in oxide of same height, which will insulate the gate

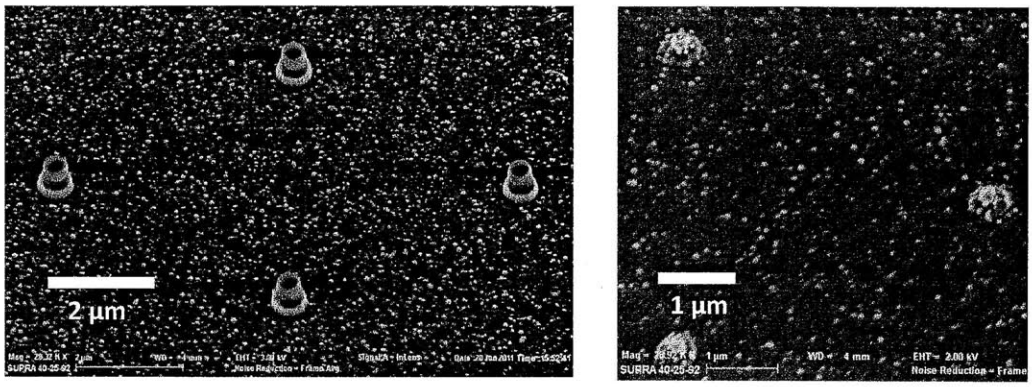

Figure 5-7: SEM images of a few pump sites after Ni and TiN etching steps. The left image shows the photoresist intact and the right shows sites after the photoresist has been removed.

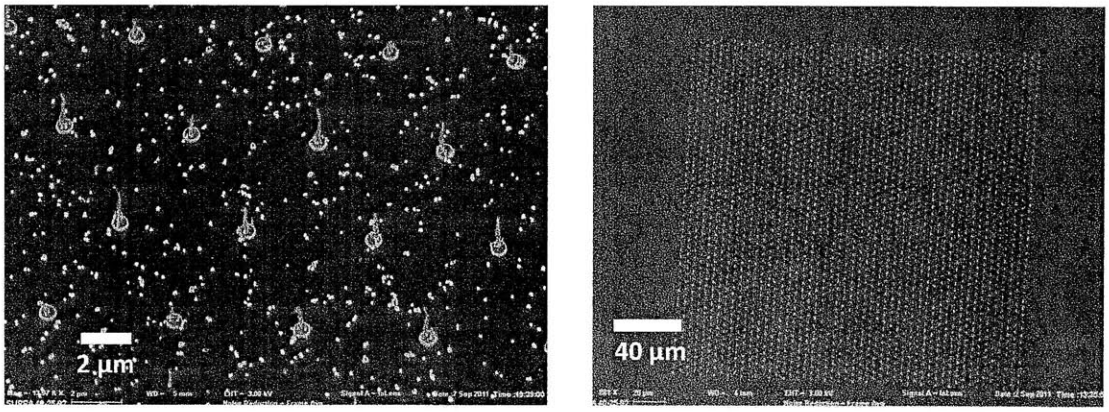

Figure 5-8: SEM images of the floral device after CNT growth

layer from the substrate. The oxide is deposited via CVD. The deposition is isotropic and causes pillars to form as seen in Figure 5-9. These pillars are polished to form a flat oxide surface via chemical mechanical polishing (CMP) on which the gate layer will reside.

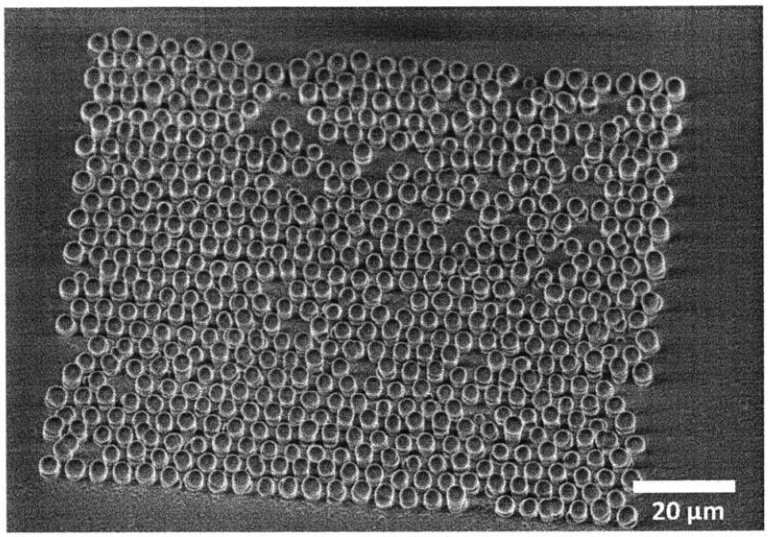

Figure 5-9: SEM images of the oxide covered CNTs on the floral device

Figure 5-10 shows the planarized surface depending for two different planarization duration using the CMP.

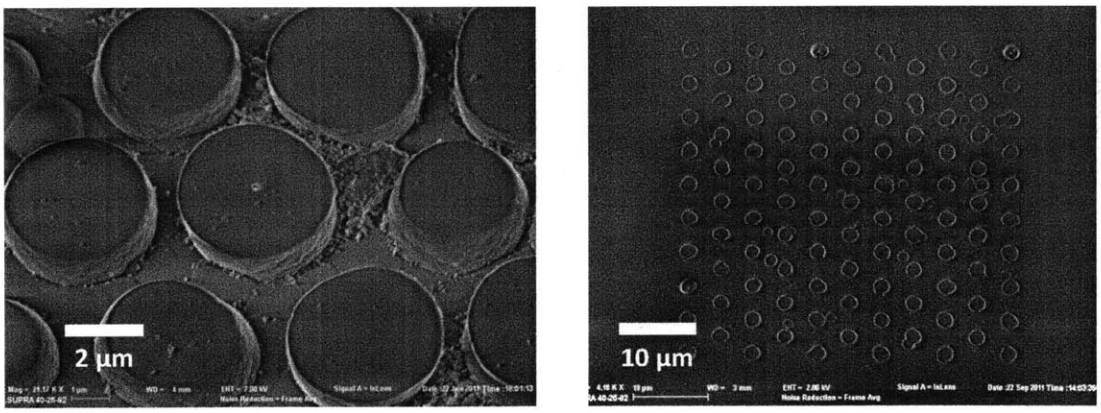

Figure 5-10: The left image shows a device after 10 minutes of CMP. 10 additional minutes of CMP yielded the device on the right.

Even though the surface may be flat, it may require more CMP processing to expose the tip of the CNTs. It is ideal for the gate layer to be in-plane with the tip of the CNT [15, 24], therefore exposing the CNT tips is preferable. Due to different heights of the CNTs some of the CNTs may become shortened due to the CMP. After sufficient number of CNTs is exposed, the wafer goes through a very quick BOE clean

to clean the oxide surface, and the 0.5 μm of phosphorous doped a-Si gate layer is deposited via CVD.

The wafer then goes through a contact lithography step to pattern the device and separate each of devices gates from one another. Double layer resist is used and the contact mask is exposed for 6 seconds. After developing, the n-a-Si layer is plasma etched until only the gate level is left, which is L-shaped in order to probe the gate without introducing stray electrostatic fields. The resist is then stripped using NanoStrip, a commercially available resist stripper. A device at this point can be seen in Figure 5-11.

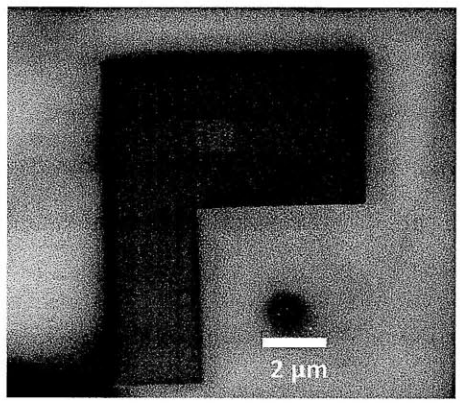

Figure 5-11: The patterned n-a-Si gate layer. The CNT ionizing area is also seen as a small square area in the middle.

A very thin layer of photoresist is then coated to pattern the aperture holes. Photoresist is spun at 6500 rpm to achieve 0.6 μm thickness of photoresist. From here the aperture pattern is exposed via photolithography, where the patterned aperture radius is 0.4 μm. After developing the resist, the device is plasma etched to create these holes, after which the resist is stripped using NanoStrip. The device undergoes a quick BOE etch in order to expose the CNT tips which are buried and surrounded by the oxide layer. The resulting device can be seen in Figure 5-12. Note that it is difficult to see the CNT as it is still slightly underneath the gate layer and the aperture holes are small. The device is now ready to be tested.

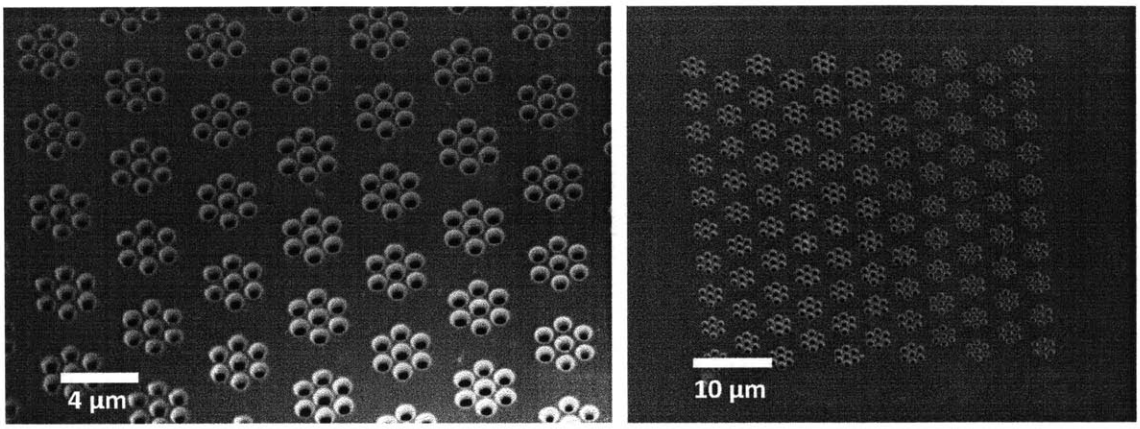

Figure 5-12: SEM images of the floral device gate structure

5.3 Self-aligned-gate Device Fabrication

Alignment error for the aperture layer along with difficulty of etching the oxide through these small aperture led to a simpler method of fabrication involving a self-aligned gate process. Most of the fabrication steps are similar to that of the floral design, though the CMP step is applied after the n-a-Si gate material is deposited. The gate material conforms to the oxide bumps seen in Figure 5-9. The underlying oxide pillars radius determines the aperture size of the gate. The CMP process polishes the pillar until the tip of the CNTs are shown. The CNT tip, oxide surrounding it and the gate material are all concentric and therefore self-aligned. The devices are defined via contact lithography as before and etched in a plasma etcher to isolate each device array from one another. A quick BOE or diluted HF dip is then used to lower the oxide level around the CNT tip. This process flow is shown in Figure 5-13.

Ni dry etching method was developed to alleviate the problems encountered during Ni wet etch. The original wet etch processing step for Ni nanodots has been one of the most inconsistent aspects of fabricating the devices. The wet etch was done by hand and the etch rate was vastly different from wafer to wafer despite having gone through the same previous steps. The color change of the wafer surface was the only indication of how far the etch had proceeded, which happened gradually. A plasma etch method for Ni was published that used a mixture of Cl_2/Ar. [44] The etch is akin to a sputter

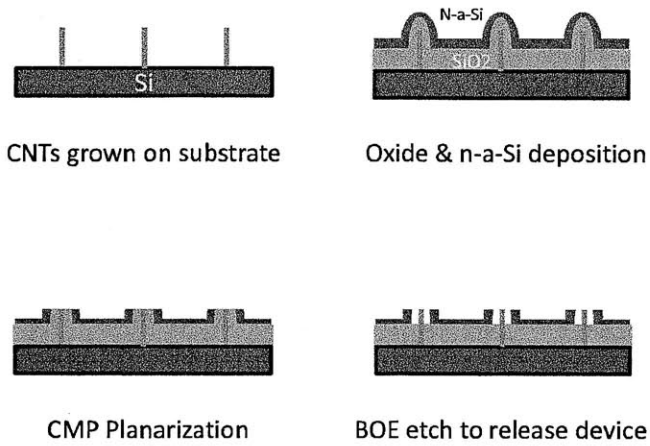

Figure 5-13: Summarized fabrication steps for the self-aligned-gate devices

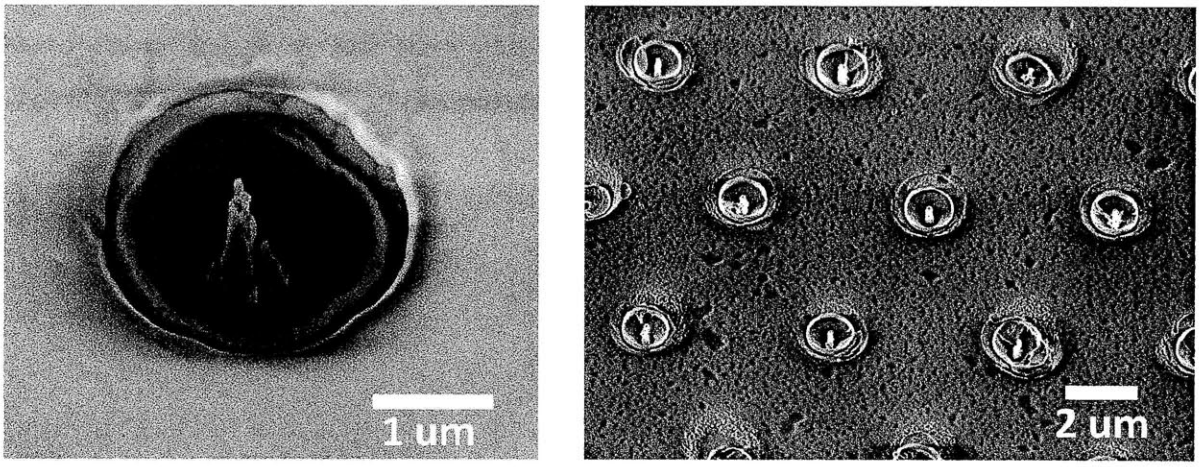

Figure 5-14: SEM images of the self-aligned-gate devices

etch therefore redeposition was a small issue. Due to different processing machine specifications, some of the parameters had to be changed as noted in Appendix B. The dry etch method alone is not enough to sufficiently reduce the size of the Ni nanodots, so a quick wet etch is needed to have the etchant undercut the nanodot and further reduce its size that will lead to single CNT growth per nanodot. This hybrid etching approach proved to be a much more reliable method of defining the Ni catalyst for CNTs. Figure 5-15 illustrates the result of this hybrid etch method.

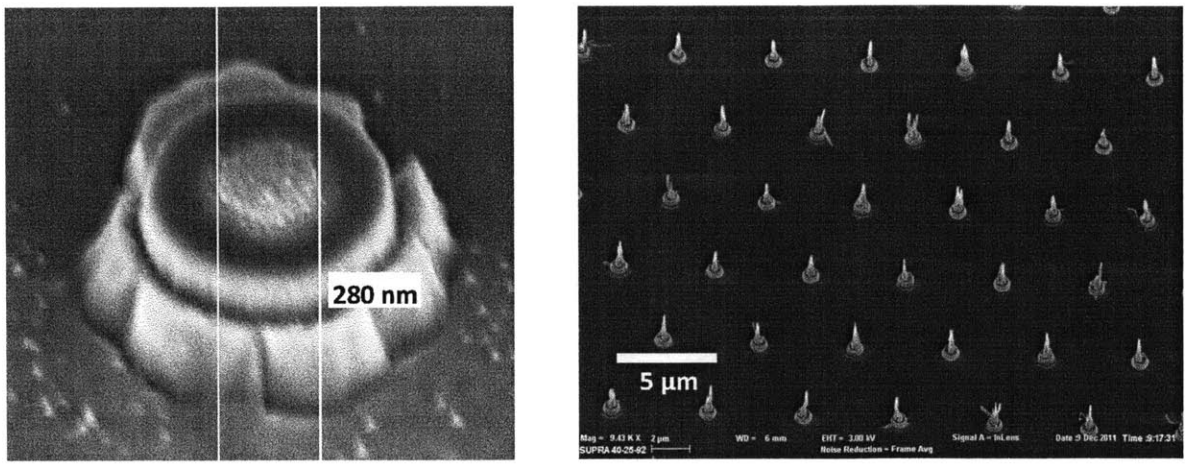

Figure 5-15: Hybrid etching method of Ni allows for an ideal amount of Ni for single CNT growth more consistently.

5.4 Discussion of the Fabrication Process

Each of the processes exhibited unique difficulties. The original horse-shoe fabrication process was the most difficult as it required the dielectric insulation layer deposited on the substrate prior to the CNT growth process. The dielectric layer charges due to ions in the plasma and subsequent arcing destroys the device as seen in Figure 5-5. The device architecture required the CNTs to grow on a layer of dielectric, and methods of eliminating the charge buildup on the dielectric layers were explored. In order to shield the dielectric from the plasma, amorphous silicon (a-Si) was deposited and patterned so the subsequent TiN deposition and patterning would completely encapsulate the oxide layer. These additional steps proved to be inadequate to completely solve the arcing issue and only made the fabrication process more complex. The a-Si layer had to be removed in the end to separate the tip and the gate electrodes, which proved to be non-trivial, as the electrode layers were narrow and long and therefore more easily affected by film stress and adhesion issues.

These reasons served as the motivation to look into other device designs. In order to circumvent the use of dielectric layers during the CNT growth process, device designs using the substrate itself as an electrode layer for the CNT ionizer were investigated. An oxide layer is deposited after the CNT growth to isolate the CNT

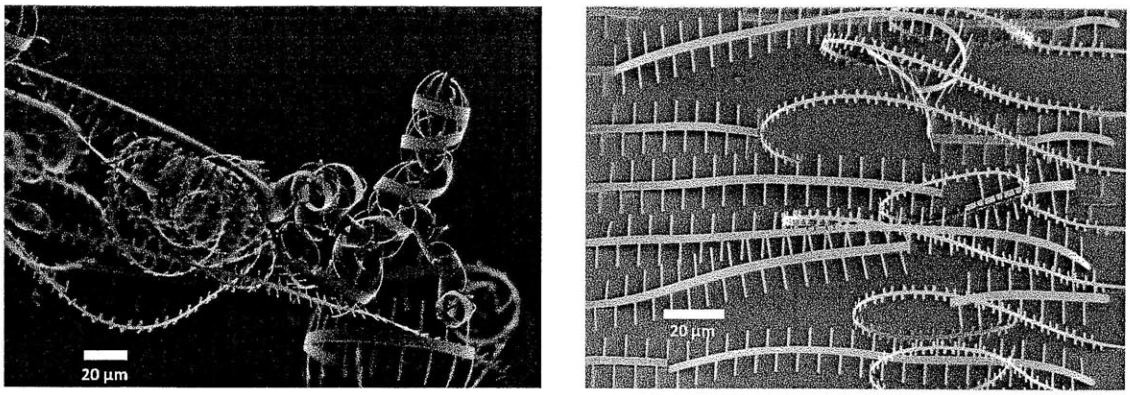

Figure 5-16: SEM of an over-etched horse-shoe device during the XeF_2 release step

and the substrate from the gate material, which would be deposited on top of the oxide layer. This layer-by-layer approach eliminated the arcing problem; however, other issues surfaced. Since a film was now used as the gate material, film stress on the gate had to be controlled. Figure 5-17 shows a device with fractures on the gate layer due to film stress during the last BOE etch release step. BOE also had trouble getting into the aperture holes to etch the oxide underneath the gate layer. Ultrasonic agitation helped with this process somewhat, and HF vapor was was explored as an alternate method of releasing the device as well.

The self-aligned gate design sacrificed the very small aperture ($\sim$ 0.4 μm) of the floral design for a simpler process that circumvented the need for very precise alignment with slightly bigger apertures ($\sim$ 0.8 μm). The use of CMP was even more critical in this design fabrication, as it would define the aperture and also the difference in height between the CNT tip and the gate. Creating pillars that would withstand the mechanical polishing step and get polished as opposed to break off was a challenge as well.

Overall the layer-by-layer approach—whether the aperture is defined with photolithography or by CMP and self-aligned—proved to be the more consistent device design. Though not without its own fabrication challenges, the simplified steps with this approach allowed a more consistent devices and needs to be explored further.

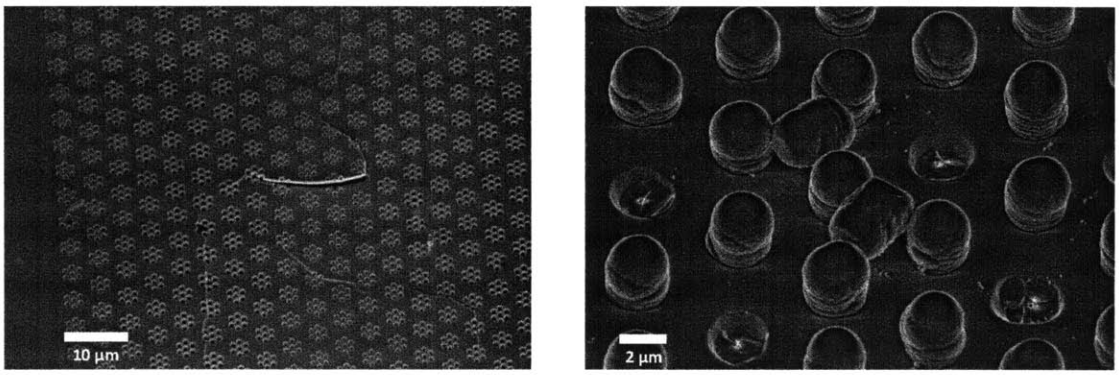

(a) (b)

Figure 5-17: (a) Stress fracture on the gate layer (b) detachment of pillars during CMP

Chapter 6

Electrical Characterization

6.1 Field Emission Characterization

The horse-shoe devices that were created successfully were characterized by running it in field emission mode. We then compared the field factor of the device to simulations and calculations.

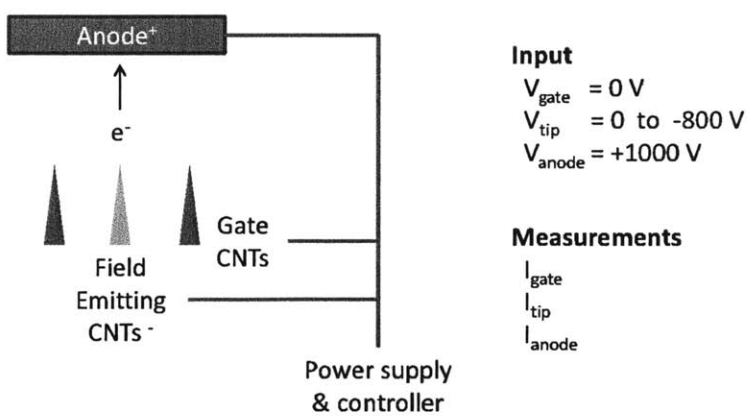

Figure 6-1: A sample electrical test setup

The device underwent a field emission test to see if the field factor is high enough for field ionization. Fowler-Nordheim analysis was done to check if the field factor

is comparable to the values obtained from modeling. The magnitude of the total emitted current should be equal to the sum of the current through the gate and the anode, and the three currents should also be directly proportional to each other — that is, if the emitted current doubles, the current captured at the gate and the anode should each double as well. Field strength of an order of magnitude higher is needed for field ionization compared to field emission, so this field emission test was done as a checkpoint to see if the device could work as a FIP. Figure 6-1 shows a schematic of an electrical characterization test setup, and Figure 6-2 shows a top-view picture of the chamber showing the probes and the anode along with the device being tested.

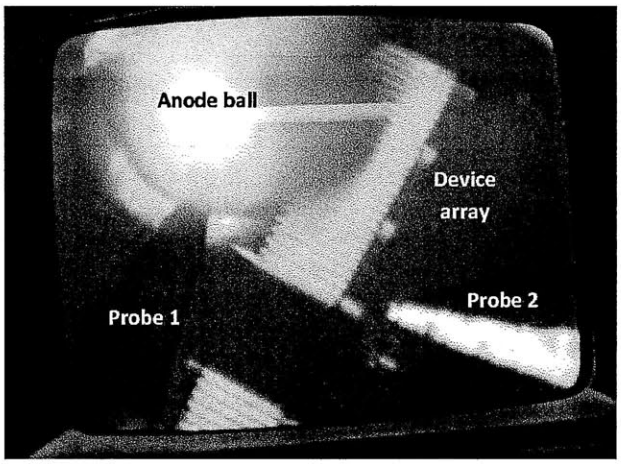

Figure 6-2: A device undergoing electrical testing. The anode ball and the two probes can be seen on the monitor.

Test results for one of the horse-shoe devices are shown below. This device called 10-O had an array of 96 field ionizers. The emitting CNT was biased from 0 V to -220 V, the anode was biased at 1100 V, and the gate was grounded. All electrical tests were done under high vacuum on the order of 10^{-9} Torr.

Most of the current was intercepted by the gate as expected, since the field lines direct the electrons from the emitting CNTs to the gate CNTs. The anode only intercepts a small portion of the emitted electrons despite being biased at 1100 V, since the distance between the tip and the gate is much smaller than the tip to the anode. Comparison of the currents is shown in Appendix C. From the anode current and the bias voltage the Fowler-Nordheim plot can be created to extract the field

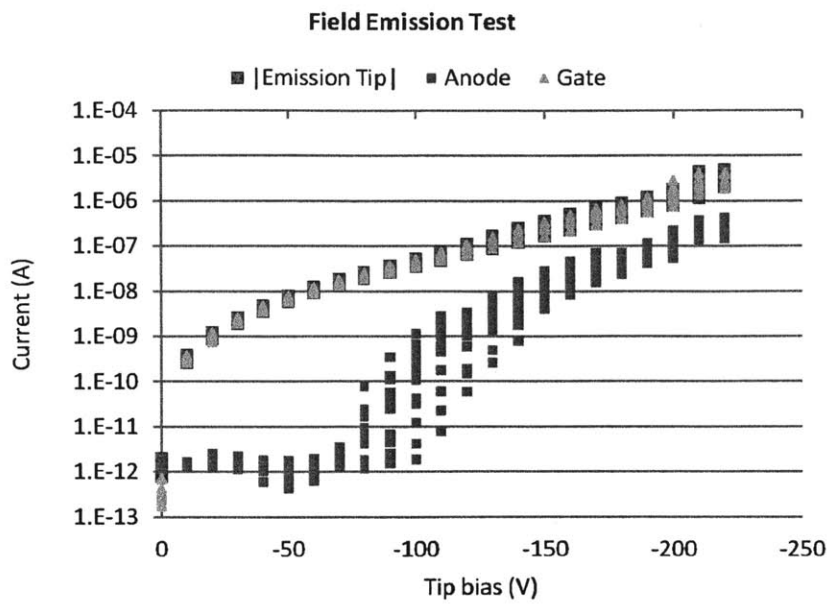

Figure 6-3: Field emission I-V curve for 10-O

factor from its slope. The plot is shown in Figure 6-4.

A separate plot is drawn only using data points with absolute bias of 100 V or above where the field emission data was much above the noise floor. Using Equation 2.11, the field factor can be extracted from this plot

$$\beta = 0.95 \cdot B \cdot \phi^{3/2}/b_{FN} \tag{6.1}$$

Using 5 eV as the work function for the CNT and $B = 6.87 \cdot 10^7\,\mathrm{VeV}^{-3/2}\mathrm{cm}^{-1}$, we get $\beta = 6.45 \cdot 10^5\,\mathrm{cm}^{-1}$. Using this estimate we can calculate that in order to produce a field strength of $1 \cdot 10^8\,\mathrm{V/cm}$, around 264 V of bias voltage would be needed. Using the rough estimation of $\beta = 1/r$ (rough, since the tested device does not have a continuous gate structure) we estimate the tip radius to be around 16 nm, which is well within the possible CNT radii created using our fabrication process. Unfortunately, confirming the device radius with SEM was impossible due to the device failure soon after the field ionization test.

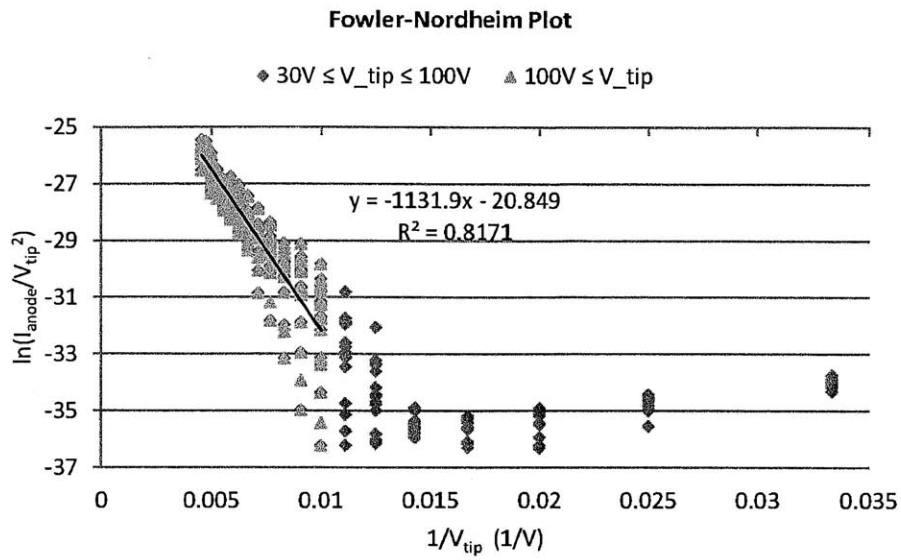

Figure 6-4: The Fowler-Nordheim plot for 10-O. Data points corresponding to absolute bias of 30 V or above were used

6.2 Field Ionization Characterization

The field ionization test was then run by biasing the tip up to 700 V while the anode was kept at -1100 V. The gate CNTs were grounded, while the pressure was kept at $5 \cdot 10^{-5}$ Torr.

As expected the field ionization current becomes measurable at a higher voltage compared to the field emission data. The noise floor is much higher for the ionizing tip on this run. The direction of the current for the anode changed due to the positive ions being implanted as opposed to the negative electrons collected during the field emission test. Some of the ions also bombarded the gate, measured as current on the gate. Note that much less of the ionization current is intercepted by the gate. This is presumably so because the ions are much heavier than the electrons and are not as strictly guided by the field lines between the ionizing tip and the gate. It is possible that the measured currents — in part or in its entirety — are due to the gate CNTs field emitting to the ionizing tip. It is less likely that the entire ionization current seen by the anode is due to field emission of the gate, as the gate current is

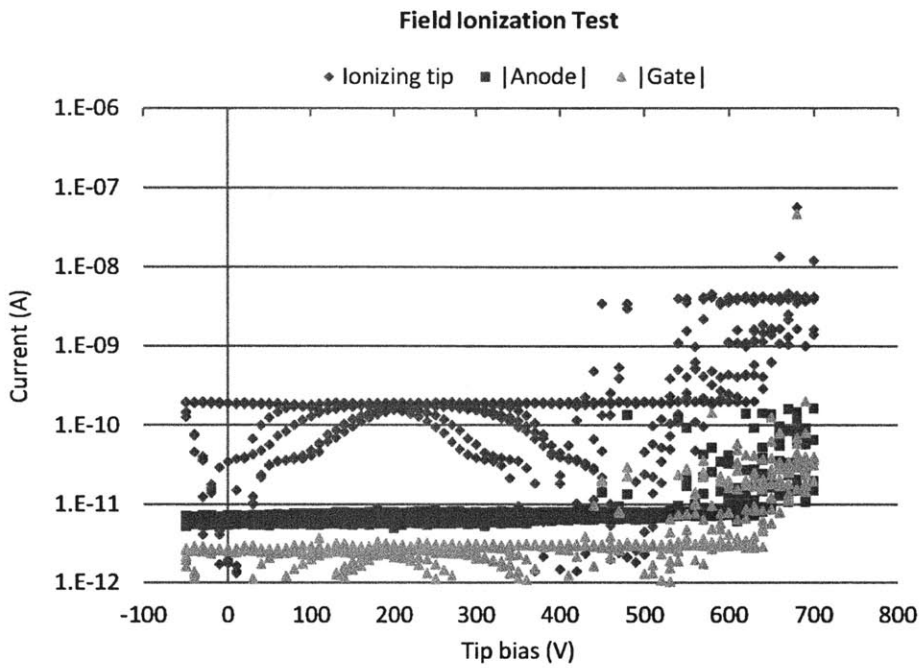

Figure 6-5: Field ionization I-V curve for 10-O

two orders of magnitude lower than that of the tip current. It is also unlikely that this current was due to FE, since a relatively large ionization region is needed for efficient ionization via EII, mainly defined by the distance between the emitters and the anode. Field emitted electrons are guided to this region to collide with the neutral molecules. In this test, the anode and the device were so close to each other, which minimized the volume of the ionization region, which in turn lowered the chance that field emitted electrons would ionize the neutral molecules. Mass spectroscopy that compares the ions created by this device in field ionization mode and another device in electron impact ionization mode could confirm field ionization over field emission in our device; the fragmentation will be much more pronounced in the electron impact ionization. This test was omitted in this thesis.

The fact that field ionization was observed at a much higher voltage of (500 V to 600 V) than expected from the FE analysis (264 V) may be due to the necessary field strength being higher than $1 \cdot 10^8$ V/cm for field ionization, or the chamber pressure ($5 \cdot 10^{-5}$ Torr) being too low for enough ionization.

Unfortunately before any other electrical or pumping tests could be done, the CNTs burned up or shorted due to excess current during a field emission test later — this was a common issue with the horse-shoe devices.

Fabrication of the layer-by-layer approach — including the floral and self-aligned-gate design architectures — was promising, though no working devices were created. In the floral devices, difficulties existed in aligning the gate aperture and release of the device by etching the oxide layer through the aperture. The simplified self-aligned gate design had difficulties with the CMP step, yielding no working devices for the thesis. Improved process flow for the self-aligned gate design should yield working devices using the layer-by-layer approach, which is left for future work.

A structure with a macro gate structure (non-micromachined) and a forrest of CNTs has also been tested for field emission and field ionization. The gap between the gate — a piece of silicon wafer — and the forrest of CNTs was around 0.5 mm. The results are shown in Appendix E.

Chapter 7

Summary & Future Work

7.1 Thesis Summary

In this thesis several different field ionization pump designs using novel architecture and fabrication processes involving photolithography patterned catalyst for the CNT growth were simulated, fabricated and tested. Electrical characterization was done on one of the device structures, which showed field ionization current of 4 nA with an array of 96 field ionizers using 700 V at $5 \cdot 10^{-5}$ Torr chamber pressure, comparable to other CNT-based field ionizers in literature. The ability to pattern the individual ionizing unit with photolithography allows for much higher throughout and results in an expedited and cost-effective process flow. A novel dry etching method was also developed with great success in creating a much more consistent process flow for the CNT growth.

Another test is done to confirm that ionized gas molecules are able to be ion implanted into the getter structure. We confirm this using X-ray photoelectron spectroscopy (XPS), which shows that ionized nitrogen molecules are found in much higher concentration in the getter structure that had gone through implantation than in a control getter that did not.

Methods of modeling a pump using field ionization has also been developed, which shows that increasing the tunneling probability — and therefore, lowering the tip radius — is the single most effective method of increasing the ionization current. The

amount of leak has a direct effect on the terminal pressure, and therefore will need to be controlled.

7.2 Suggestions for Future Work

Successful field ionization was shown in this thesis, though pumping tests are left as future work. A full pumping characterization will need to be done in varying conditions of pressures and gas composition as well as bias voltages to see if the performance of the ionization and getter structures is comparable to simulation results. A schematic of this test setup is seen in Figure 7-1. In order to be sure that the ionization of molecules is due to FI, the pumps ionizers will ionize different gasses and compare the ion composition to that of electron impact ionization.

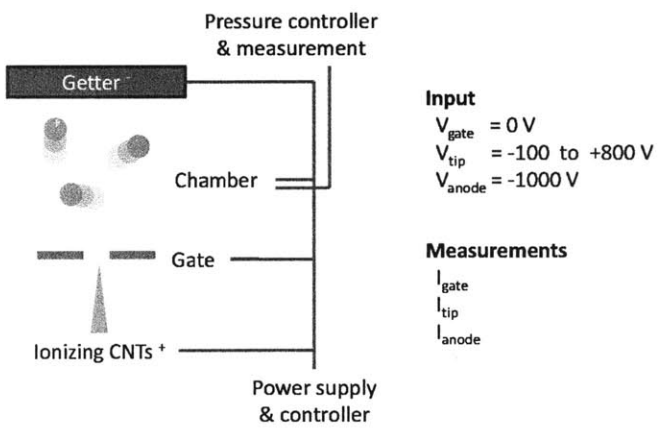

Figure 7-1: Schematic of a sample pump test setup

For the pumping test, a smaller chamber must be created to test the pumping ability of the device. A picture of such chamber is shown in Figure 7-2.

Mass spectrometry can be done using the device array as a field ionizer and as a field emitter to compare the spectrometry results. Because of the difference between the two ionization phenomena, the resulting composition of ions will look different, which gives confidence to the case that field ionization had been the ionization source.

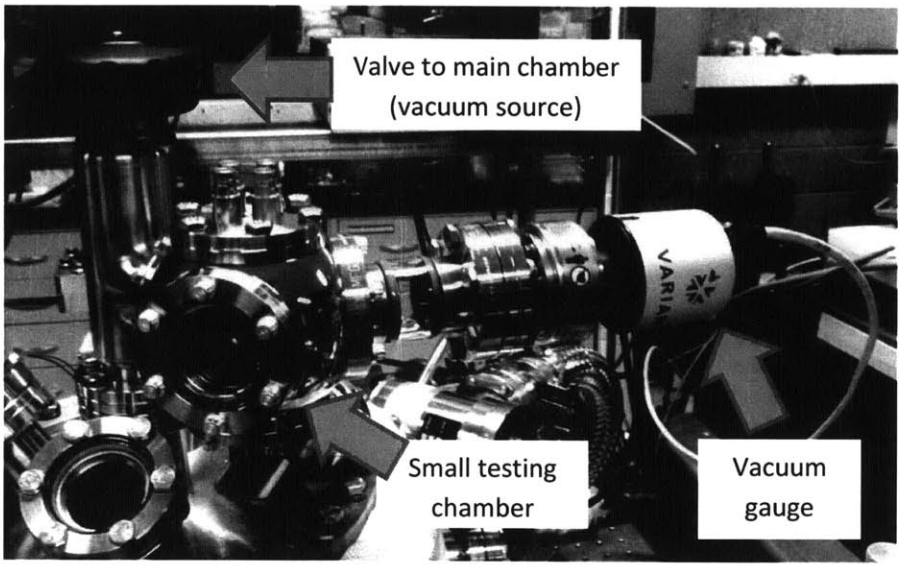

Figure 7-2: Pump test setup. A smaller bulbous chamber is used to house the FIP and a pressure gauge can be seen connected to the right. A valve isolates this small chamber from the big load lock chamber used to set the initial pressure.

This device can be packaged in a pump with test setup to measure the pressure of the chamber in which the field ionization array pump is enclosed. Leakage tests may be performed as well for this enclosure. Packaging will be another challenge for the project as it will need to interact with different pumps such as the mechanical pump that will pump to low-vacuum, allowing the field ionization array to start pumping down.

Getter material selection and design, as well as its integration with the ionizers will need to be explored. Its performance such as capacity and the effect of ions mass on implantation probability should be characterized as well.

After the FIPs ability to pump is shown, it will need to be integrated with the other pump elements such as the valves and the mechanical rough pump. Various methods of encapsulation and robust integration methods will need to be explored and its performance characterized.

Appendix A

Mask Layouts

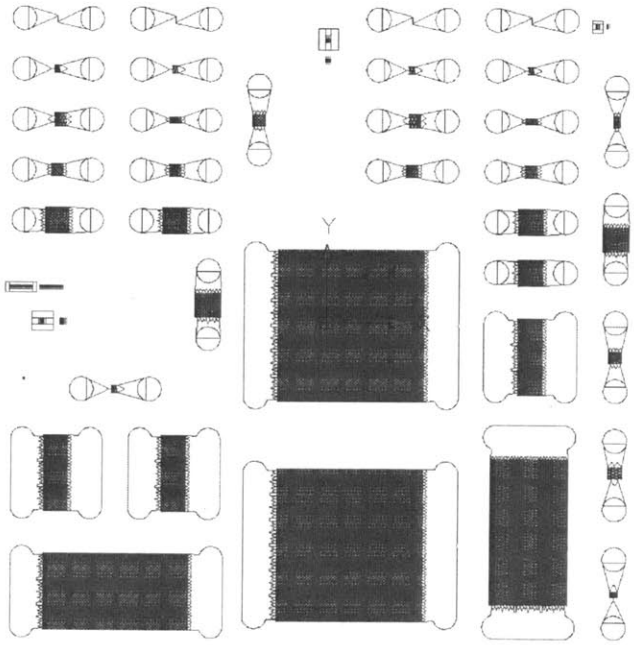

Figure A-1: Mask layout of the horse-shoe design: electrode layer

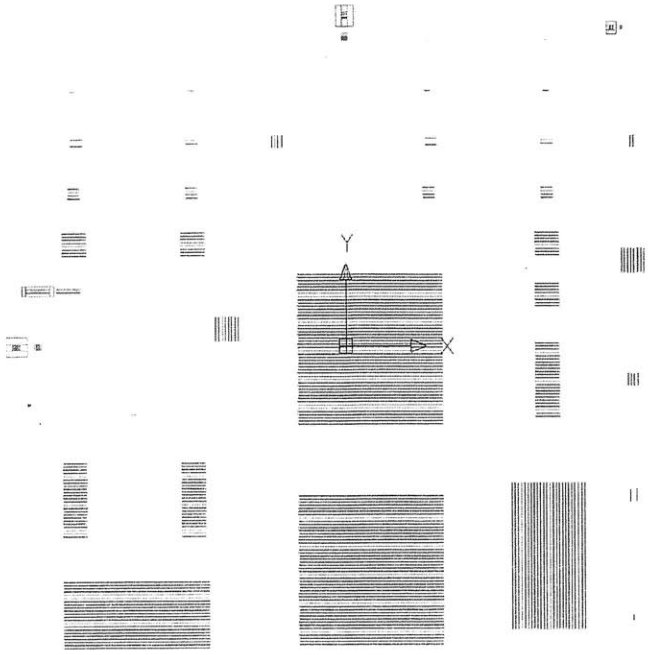

Figure A-2: Mask layout of the horse-shoe design: nanodot catalyst layer

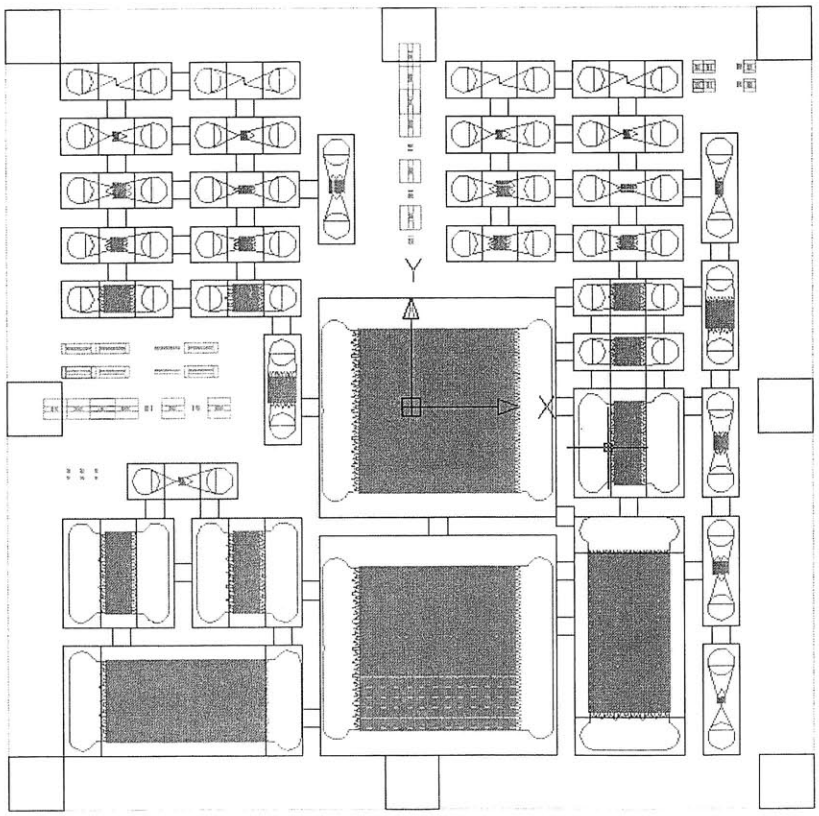

Figure A-3: Mask layout of the hose-shoe design: all layers

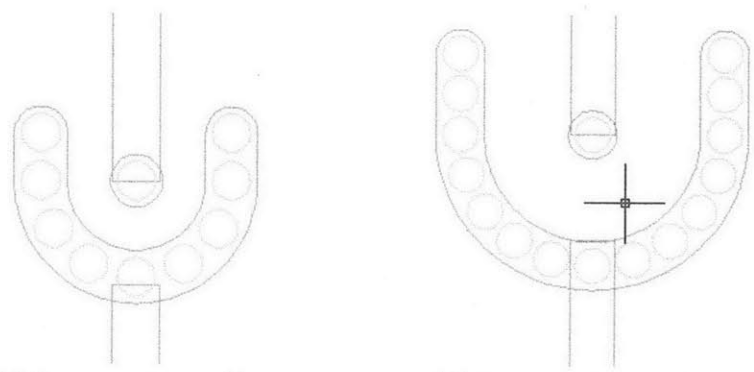

(a) 2 μm aperture radius (b) 3 μm aperture radius

Figure A-4: The two different aperture radii for the gate structure in the mask layout

Appendix B

Process Flows

Horse-shoe design process flow

	Process step	Process Tool	Comments
	Start with 6" n-type Si wafer		
Pattern alignment marks			
1	Coat with photoresist	coater6 [ICL]	*T1 HMDS* recipe
2	Expose alignment mark	i-stepper [ICL]	"First" alignment, 160ms exposure
3	Develop	coater6 [ICL]	*PUDDLE3*
4	Etch alignment mark	AME5000 [ICL]	Baseline-poly, 180s etch
5	Ash photoresist	asher [ICL]	
Base layer deposition			
6	RCA clean	RCA [ICL]	
7	PECVD 2μm SiO_2	DCVD [ICL]	
8	PECVD 50nm a-Si	DCVD [ICL]	
9	Anneal wafer	5B-Anneal [ICL]	1 hour anneal
10	Pattern cavity pattern: coat PR, Expose, Develop	coater6, i-stepper , coater6 [ICL]	
11	Anisotropic etch of a-Si and SiO for 20nm	AME5000 [ICL]	
12	Ash photoresist	asher [ICL]	
CNT creation			
13	Pre-metal clean	Piranha / premetal clean [ICL]	Piranha + HF dip
14	PVD 50nm TiN	Endura [ICL]	*TiN 500A* as diffusion barrier and conduction layer
15	Pattern conduction paths for tip and gate: coat PR, Expose, Develop	coater6, i-stepper , coater6 [ICL]	
16	Etch conduction layer	Rainbow [ICL]	*DJANG-TIN-TIMED:* 20% Ar/Cl_2 for 5m
17	Ash photoresist	asher [ICL]	
18	Evaporate Ni layer	ebeamCMOS [ICL]	20nm Ni deposition
19	Pattern CNT catalyst on tip and gate	coater6, i-stepper , coater6 [ICL]	
20	Etch catalyst layer with ultrasonication	Acid-hood [TRL]	Transene Ni etchant, room temperature, Ultrasonification, etch for 5s longer after complete color change
21	Strip photoresist	asher [ICL]	
22	Grow CNT	CCNT [TRL]	Annealing & deposition in CNT reactor. 770 degrees, 180W 700V DC plasma power, 15min deposition

Floral design process flow

	Process step		Process Tool	Comments
	Start with 6" n-type Si wafer			
Pattern alignment marks				
1	Coat with photoresist		coater6 [ICL]	*T1HMDS* recipe
2	Expose alignment mark		i-stepper [ICL]	"First" alignment, 160ms exposure
3	Develop		coater6 [ICL]	*PUDDLE3*
4	Etch alignment mark		AME5000 [ICL]	*Baseline-poly*, 180s etch
5	Ash photoresist		asher [ICL]	
CNT creation				
6	Pre-metal clean		Piranha / premtal clean [ICL]	Premetal clean w/ 30s 50:1 HF dip
7	PVD 50nm TiN		Endura [ICL]	*TiN 500A* as diffusion barrier
8	Anneal TiN layer		RTA2 [ICL]	*800d30s* to improve film quality
9	Ebeam deposition 20nm Ni for CNT catalyst		ebeamCMOS [ICL]	2A/s deposition rate
10	Pattern CNT catalyst:	coat PR Expose Develop	coater6 i-stepper coater6 [ICL]	*T1HMDS* 120ms exposure *PUDDLE3*
11	Etch Ni layer		Acid-hood [TRL]	Transene Ni etchant, room temperature, Ultrasonification, etch for 5s longer after complete color change
12	Plasma etch TiN		Rainbow [ICL]	*DJANG-TIN-TIMED:* 20% Ar/Cl_2 for 5m
13	Ash PR		Asher [ICL]	
14	Grow CNT		CCNT [TRL]	Annealing & deposition in CNT reactor. 770 degrees, 180W 700V DC plasma power, 15min deposition
Gate formation				
15	PECVD Oxide to CNT height		STS-CVD [TRL]	*LF-SIO* (85nm / min)
16	CMP oxide to planarize the oxide layer		GnP [ICL]	1μmper 10min
17	BOE to clean oxide surface		Acid-hood [TRL]	7:1 BOE etch for 15s
18	30nm n-a-Si deposition		STS-CVD [TRL]	*DOPED-SI* for 4min
19	Contact lithography:	Coat PR Expose Develop	Coater EV1 Acid-hood [TRL]	Double coat resist OCG825, Develop using OCG934
20	Etch to define devices		SAMCO [TRL]	*Recipe #20* for 3 cycles
21	Strip PR		Acid-hood [TRL]	Heated Nanostrip solution
22	Coat PR		Coater	OCG825 at 6k rpm for

			0.6μm thickness
23	Expose aperture pattern	i-stepper [ICL]	250ms exposure
24	Develop	Acid-hood [TRL]	OCG934
25	Etch gate aperture	SAMCO [TRL]	*Recipe #20* for 4 cycles
Release device			
26	BOE etch to release device	Acid-hood [TRL]	7:1 BOE etch for 10min with ultrasonification
27	Strip PR	Acid-hood [TRL]	Heated Nanostrip solution

Self-aligned-gate design process flow

	Process step		Process Tool	Comments
Same as steps 1-14 in Floral design process flow				
Gate formation				
15	PECVD Oxide to slightly less than CNT height		STS-CVD [TRL]	*LF-SIO* (85nm / min)
16	0.4μm n-a-Si deposition		STS-CVD [TRL]	*DOPED-SI* for 6min
17	CMP until CNT tips are seen		GnP [ICL]	1μmper 10min
18	Contact lithography:	Coat PR Expose Develop	Coater EV1 Acid-hood [TRL]	Double coat resist OCG825, Develop using OCG934
19	Etch to define devices		SAMCO [TRL]	*Recipe #20* for 3 cycles
20	Strip PR		Acid-hood [TRL]	Nanostrip solution
Release device				
21	BOE etch to release device		Acid-hood [TRL]	7:1 BOE etch for 10min with ultrasonification

Dry/wet hybrid Ni etch CNT growth process flow

	Process step	Process Tool	Comments
Same as steps 1-5 in Floral design process flow			
CNT creation			
6	Pre-metal clean	Piranha / premtal clean [ICL]	Premetal clean w/ 30s 50:1 HF dip
7	PVD 50nm TiN	Endura [ICL]	*TiN 500A* as diffusion barrier
8	Anneal TiN layer	RTA2 [ICL]	*800d30s* to improve film quality
9	Ebeam deposition 20nm Ni for CNT catalyst	ebeamCMOS [ICL]	2A/s deposition rate
10	Pattern CNT catalyst: coat PR Expose Develop	coater6 i-stepper coater6 [ICL]	*T1HMDS* 120ms exposure *PUDDLE3*
11	Sputter (dry) etch Ni layer	Rainbow [ICL]	*Ni-dry-test:* 50mTorr,100W/400W RF_f/RF_b, 20% Ar/Cl_2 for 3m
12	Plasma etch TiN	Rainbow [ICL]	*DJANG-TIN-TIMED:* 20% Ar/Cl_2 for 5m
13	Wet etch Ni	Acid-hood [TRL]	Transene Ni etchant for 5s
14	Ash PR	Asher-Matrix [TRL]	
15	Grow CNT	CCNT [TRL]	

Appendix C

Sensitivity Analysis of the Model

Baseline (BL) columns are bolded

Temperature (T)

T (K)	**300**	150 (-50%)	270 (-10%)	330 (+10%)	450 (+50%)
$1/T$ (K^{-1})	**0.0037**	0.00667	0.00333	0.00303	0.00222
Ratio to BL	**1**	2	1.11	0.91	0.67

Ionization volume (ν)

Fixed parameters: tip bias (V_g): 500 V

r (nm)	**20**	30 (+50%)	40 (+100%)
ν (nm^3)	**2.82 E4**	7.06 E4	1.21 E5
Ratio to BL	**1**	2.50	4.29

Tunneling probability (D)

Fixed parameters: tip bias (V_g): 500 V, CNT workfunction (ϕ): 5 eV

β (cm^{-1})	**5 E5**	2.5 E5 (-50%)	4.5 E5 (-10%)	5.5 E5 (+10%)	7.5 E5 (+50%)
D	**7.37 E-7**	5.43 E-13	1.54 E-7	2.66 E-6	8.16 E-5
Ratio to BL	**1**	7.37 E-7	0.21	3.61	110.71

Tunneling probability (D)

Fixed parameters: tip bias (V_g): 500 V, field factor (β): 5 E5 cm^{-1}

ϕ (eV)	**5**	4.5 (-10%)	5.5 (+10%)
D	**7.37 E-7**	4.70 E-7	1.18 E-6
Ratio to BL	**1**	0.64	1.60

Appendix D

Electrical Characterization of the Horse-shoe Device (10-O)

As the emission current varied due to the different amount of biasing from 0 to -220 V, the gate and the anode currents varied linearly with it. Around 90% of the electrons emitted from the tip CNT was captured by the gate CNTs, whereas 8.6% was captured by the anode. The fact that most of the electrons are captured by the gate is a not an issue and was expected for this test as this device will use field ionization rather than electron impact ionization.

In order to estimate the noise level from the electrical test setup and equipment, a test run was done with the probes disconnected from the device. Probe 1 was biased from 0 to -900 V. Noise level was near the nA range for higher biases. It is possible that the probe itself was field emitting.

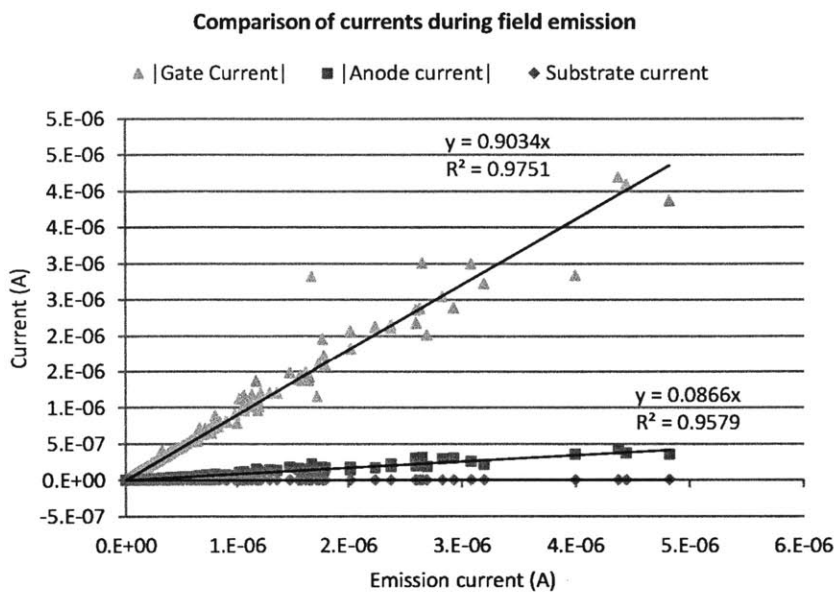

(a)

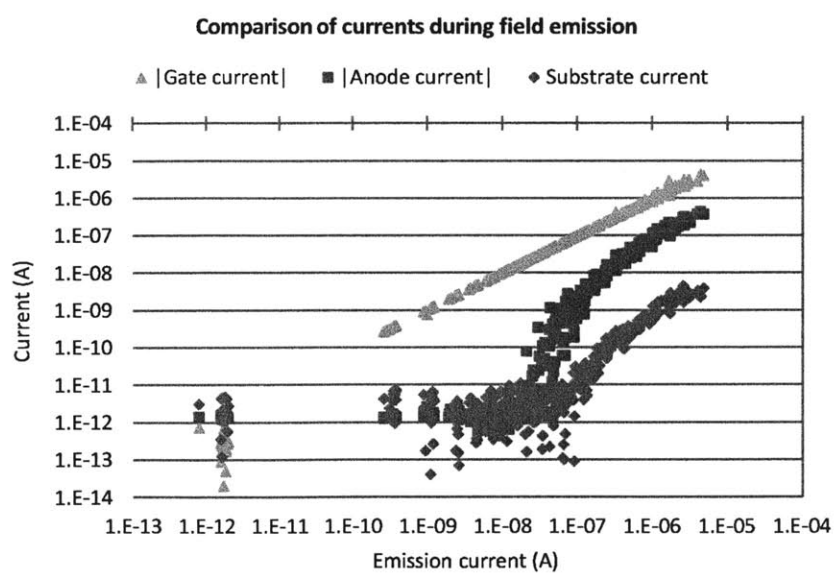

(b)

Figure D-1: Gate, anode and substrate currents compared to the emission current for 10-O: (a) linear plot; (b) log-log plot

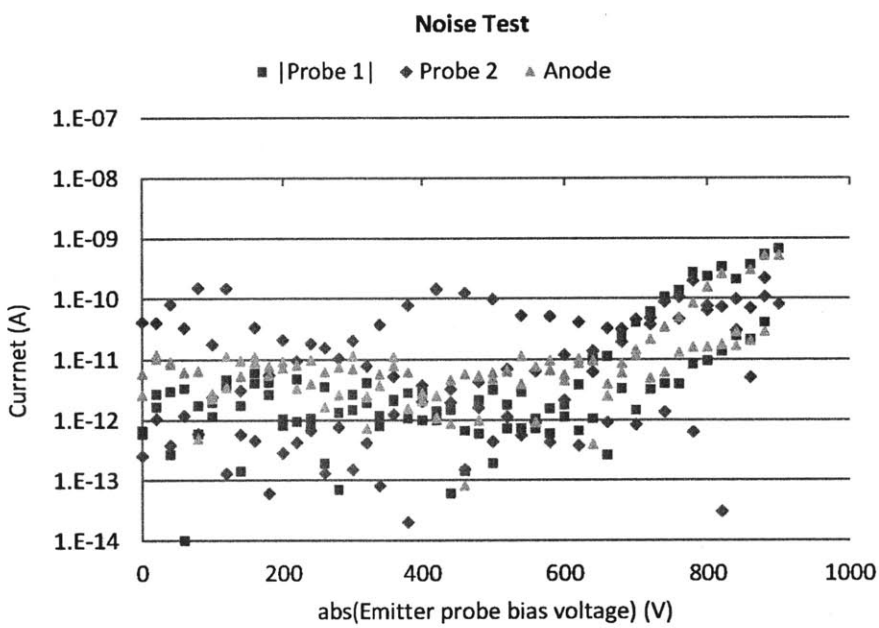

Figure D-2: Noise test using the electrical test setup

Appendix E

Electrical Characterization of the Macro Device

A 1 cm^2 wafer piece with a CNT forrest went through FE and FI characterization. The gate structure was not fabricated on top of the piece but rather a piece of silicon placed on top of the CNT forrest piece with about 0.5 mm gap. The silicon piece was dipped in HF prior to installing it on the testing setup to reduce the amount of native oxide present. This gate structure acted also as the anode and the getter for testing. For both FE and FI characterization the CNTs were grounded while the gate/getter piece was biased.

The performance of this forrest device will benefit greatly from the high density of CNTsin this 1 cm^2 forrest the number of CNTs is estimated to be in the range of 10^9 to 10^{10}. There are several factors which will lower the performance, however. Lower field factors are expected at the tips of the CNTs due to the proximity of each tip to one another, which leads to the screening effect and lower field factor. [45, 46] There is much variation in the tip radius for the CNTs with the majority being much larger than the individually patterned CNTs. The gate structure is placed much farther from the CNTs compared to the micromachined gate structures, further lowering the field factor, though this is also an advantage, as higher biases can be used with no fear of dielectric breakdown and the possibility of arcing is much reduced.

The gate/getter structure was biased from 0 to 500 V to test its FE characteri-

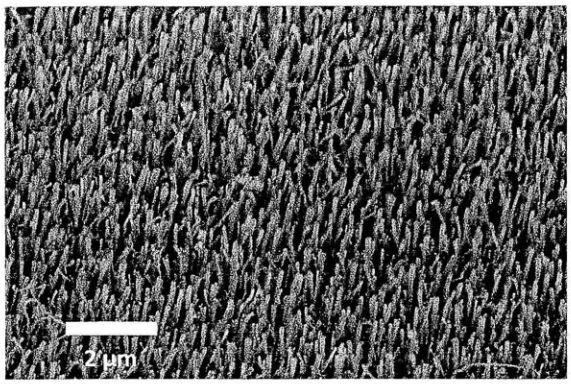

Figure E-1: SEM image of the CNT forrest growth

zation. Turn-on was exhibited little over 200 V. At 500 V bias the emitted current was nearly $1 \cdot 10^5$ A. Most of the emitted current was captured by the gate/getter structure as seen in Figure E-3.

The Fowler-Nordheim plot is seen in Figure E-4. The field factor corresponding to the slope of the FN plot is $1.47 \cdot 10^5\,\mathrm{cm}^{-1}$, which corresponds to CNT tip radius of 68 nm.

The FE performance of this forrest can be compared to commercially available field emitters such as the CNT cathodes made by Busek Inc. The cathode uses a forrest of randomly oriented CNTs as the emitter and is able to emit 0.6 mA with 470 V bias in its TO-5 package [47, 48]. The emitter area is enclosed by a circular packaging with 10 mm diameter, which is approximately 0.8 cm^2. The gate structure is a metal grid with 70% porosity placed 100 μm above the emitters. This gate proximity may explain the difference in performance between Buseks cathode and the CNT forrest device we tested.

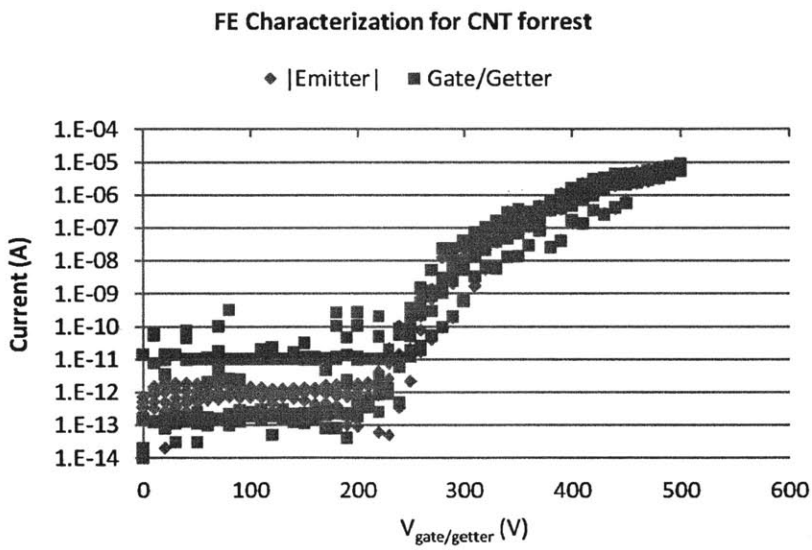

Figure E-2: Macro test I-V curve of the FE test with the forrest CNTs

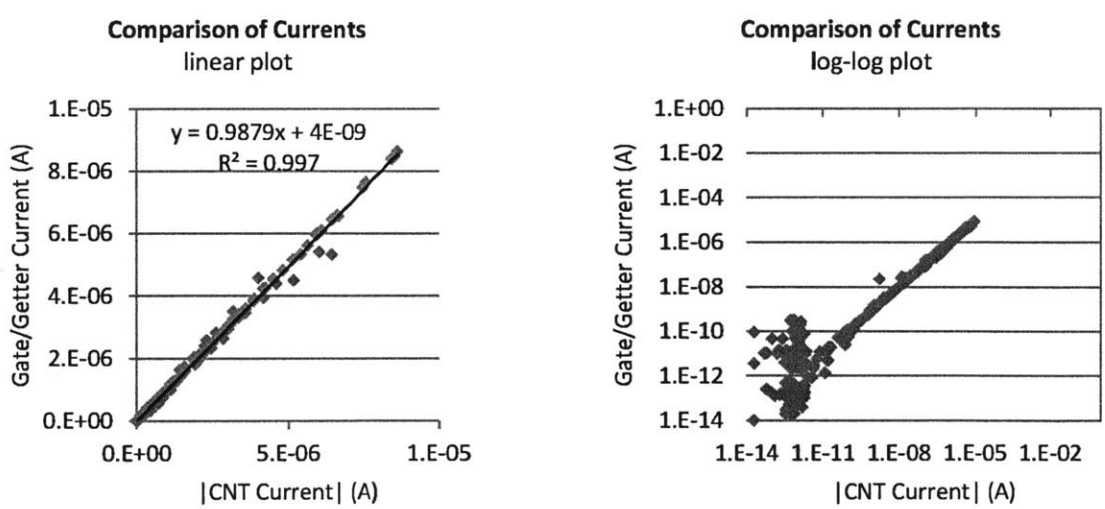

(a) (b)

Figure E-3: Comparison of the emitted current to the gate/getter current for the FE test with a forrest of CNTs

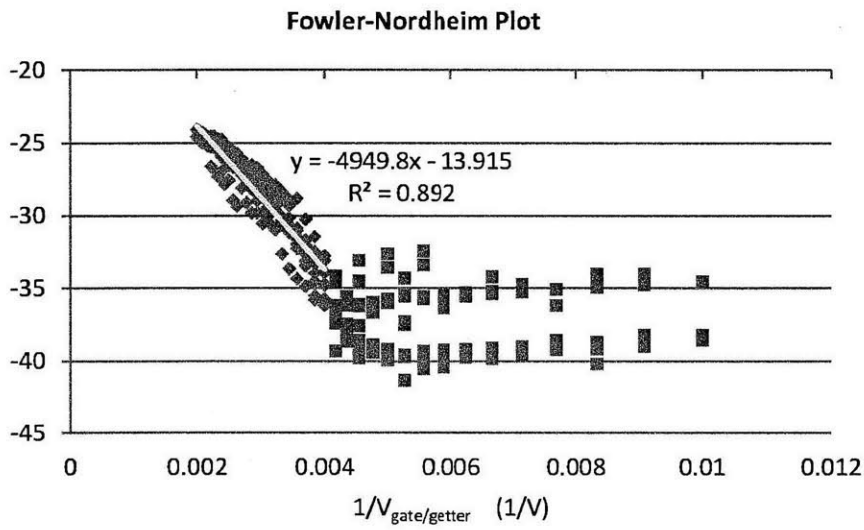

Figure E-4: Fowler-Nordheim plot for the FE test with a forrest of CNTs

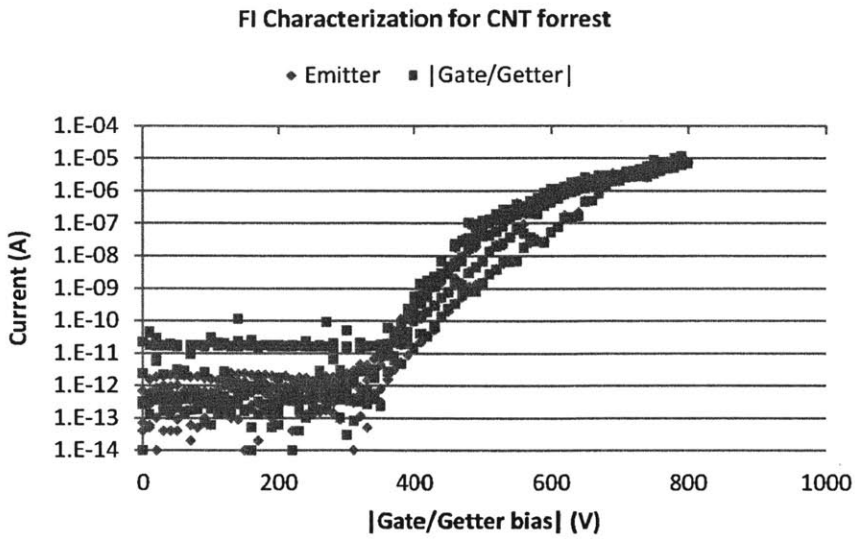

Figure E-5: FI characterization of the forrest of CNTs

The field ionization test was done by lowering the bias on the gate/getter structure while the CNTs were grounded. The I-V curve is shown in Figure E-5. Most of the ions created through field ionization are captured by the getter. Note that the turn-on voltage for the field ionization is around 300 V, which is higher than that of field emission by about 100 V. Higher bias of 630 V is needed to attain ionization current of $1 \cdot 10^6$ A through FI, whereas only 400 V is needed for FE.

In order to verify that the observed current during the FI test was legitimately due to FI and not due to the getter structure emitting current, a FE/FI run was done where the CNT forrest was replaced by a 1 cm^2 square silicon piece. Bias of $\pm$ 1000 V yielded current level no more than the noise floor (<100 pA). In order to see if the ionized gases were implanted in the getter structure, the device was biased at 1000 V for 1 hour. Visual inspection of the getter yielded a discolored surface, as seen in Figure E-6.

X-ray photoelectron spectroscopy (XPS) was done on the surface of the getter to confirm the composition of the implanted material. As a comparison, the spectroscopy was done on two separated areas on the getter as well as one area on a control piece that did not go through the field ionization experiment but stored in the same

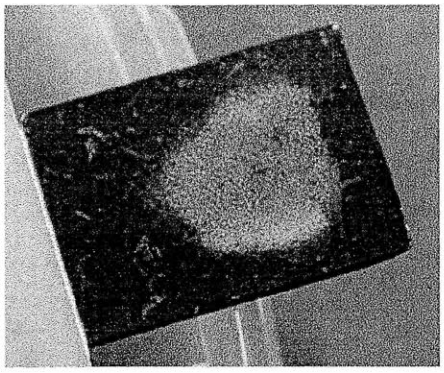

Figure E-6: The discolored getter piece after the field ionization run

environment. The results from the XPS is shown in Figure E-7.

Higher concentrations of atmospheric gas elements would be expected on the rough area of the test piece. The concentration of Nitrogen, which comprises of 78% of the atmosphere, would be most notably increased in this area, which is the case. The atomic concentration of the surface scans is shown below as well:

	Control	Test (smooth)	Test (rough)
Si 2s	40.7%	21.9%	10.8%
O 1s	35.6%	27.6%	13.8%
C 1s	17.1%	43.2%	48.1%
Cl 2p	2.0%	1.4%	0.4%
N 1s	0.9%	2.8%	13.8%

The surface compositions of the control piece and the smooth area of the test piece show that the environmental factors such as contamination and the effects of storage did not change either pieces compositions by much. The rough area deviates from the other two compositions with much higher Nitrogen concentration, which shows that field ionization of the atmospheric gases and the implantation of the ionized molecules into the getter were successful for the macro FIP test.

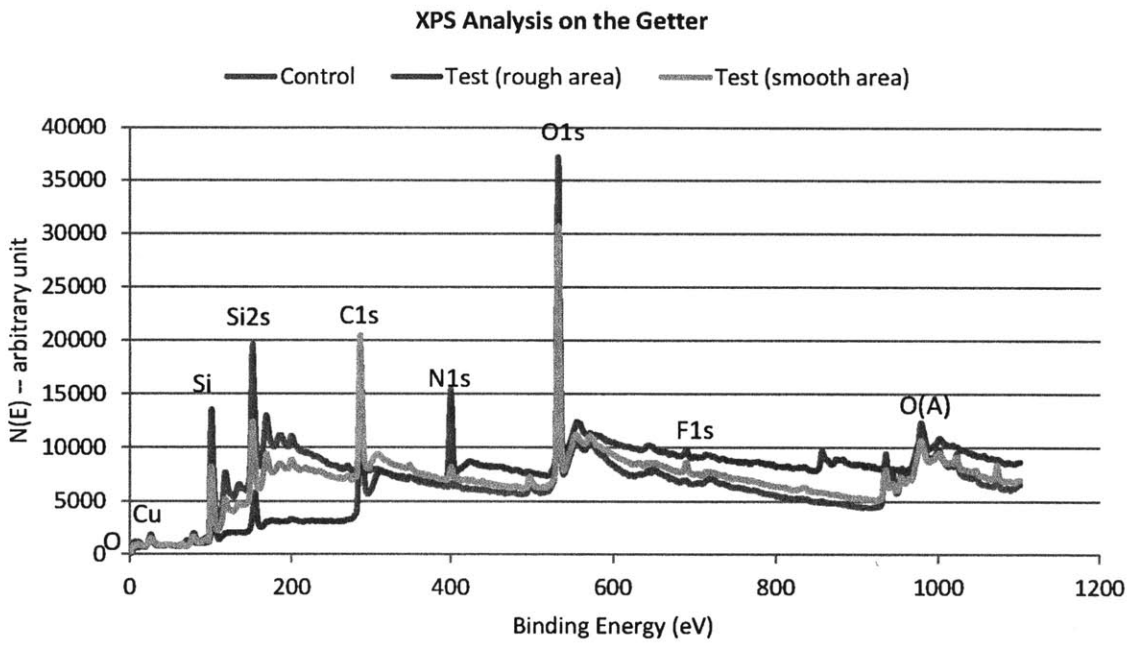

Figure E-7: I-V curve for the macro FIP test with a forrest of CNTs

Appendix F

MATLAB Code

ficurrent.m

```
function ficurrent
addpath('D:\My Dropbox\M.Eng\Simulations\MATLAB\');
close all

correction = 1;
f=1e15;
D=calc_D_func(5e5,570);      % calc_D_func(beta, voltage)
                             % Chen gets 5e5 field factor -- experimental

% lamda=1.3e-22;  % ~ 8nm sphere on 40nm tip
% lamda = ion_volume(500);        % assumes r40nm p0.4um
lamda = 2.8e-23;     % estimate for chen

emitters=30;     % emitters=1e4;
Volume=20e-9;    % 20 mm^3
q=1.6e-19;
k=1.38e-23;      % boltzmann constant
temperature=300;

n=(100000000:-1000:1000)*1e6;    % number of molecules

Pressure=(n*temperature*k/Volume)/133; % 133 is Pa --> Torr conversion

Ii=q*n*lamda*emitters*f*D/Volume*correction;

% plot(Pressure,Ii,'o');
loglog(Pressure,Ii,'o');
xlabel('Pressure (Torr)')
ylabel('Ion Current (A)')
title('Total Ion Current vs Pressure')
```

calc_D_func.m

```
function d=calc_D_func(beta,V_g)
% Calculating D (tunneling probability)

% beta = 2e5;          % field factor in cm^-1
% V_g = 500;          % gate voltage in V
F = beta * V_g;      % field strength in V/cm

% I_n = 15.58;         % N2's
% I_ar = 15.76;        % Ar's
I_o = 12.06;         % O2's
            %-- http://www.opticsinfobase.org/abstract.cfm?id=53040

I = I_o;

B = 6.87E7; % constant B in V*eV^(-3/2)*cm^(-1)

phi = 5; % work function of Carbon in eV
            %-- http://linkinghub.elsevier.com/retrieve/pii/S0008622300003225

% d = exp(-B*2*(I-phi)/F/(2*I-phi)*(I.^(3/2)-(phi/2)^(3/2)));     % other D

d = exp(-B/F*(I-phi)*I^(0.5));       % updated D
```

ion_volume.m

```
function V = ion_volume(voltage,ionization_threshold)
% voltage applied to tip -- can be an array
% threshold field strength for ionization in V/m. default = 1e10 V/m

if nargin < 2, ionization_threshold = 1e10; end

load('Maxwell_Data_FIPv2.mat','data');     % data of r40nm 1V p0.4um
data = data(58:end/2,:);                   % truncate the repeated 1/2 of field
data

data_r = data(:,1);                        % extract radius data
data_f = data(:,2) * voltage;              % extract & multiply by bias

% data = [data(:,1),data(:,2)*voltage];     % get field for voltage applied

[~, where] = min(abs(data_f-ionization_threshold));   % find closest radius
to given threshold

threshold_radius = zeros(length(voltage):1);

for i = 1:length(voltage)
    threshold_radius(i)=data_r(where(i));
end

V = 4/3*pi*((threshold_radius).^3-40^3)*(10^-27) / 2;  % volume of half shell
in m^3



% plot
if (length(voltage)>1)
    figure;
    subplot(211);plot(voltage,threshold_radius);title({'Ionization Volume
Calculation';'r = 40nm, p = 0.4um';'';'Ionization radius'});xlabel('Tip
voltage [V]');ylabel('Ionization shell radius [nm]');
    subplot(212); plot(voltage,V,'r');title({'Ionization Volume';'Half of
spherical shell'});xlabel('Tip voltage [V]');ylabel('Ionization volume
[m^3]');
end
```

ion_volume_r30.m

```
function V = ion_volume_r30(voltage,ionization_threshold)
% voltage applied to tip -- can be an array
% threshold field strength for ionization in V/m. default = 1e10 V/m

if nargin < 2, ionization_threshold = 1e10; end

load('Maxwell_r30nm.mat');            % data of r30nm 1V p0.4um
data = r30nm;

data_r = data(:,1);                    % extract radius data
data_f = data(:,2) * voltage;          % extract & multiply by bias

[~, where] = min(abs(data_f-ionization_threshold));   % find closest radius
to given threshold

threshold_radius = zeros(length(voltage):1);

for i = 1:length(voltage)
    threshold_radius(i)=data_r(where(i));
end

V = 4/3*pi*((threshold_radius).^3-20^3)*(10^-27) / 2;  % volume of half shell
in m^3
```

fint2.m

```
  function fint2

n0=2e16;      % n in 30 torr 20mm3 --> 30*133*20e-9/1.8e-23/300
leakage = [1e-4,1e-5,1e-6];  % in mm^3/s

k=1.38e-23; %boltzmann constant
temperature=300;

nleakage=760*133*leakage*10^-9/(k*temperature);

correction = 1;
fexp=1e15/10^7;              % f*D
lamda=ion_volume(1000);      % 1000V tip voltage
emitters=1e3*50;             % 50000 emitters
Volume=20e-9;
tao=1/(lamda*emitters*fexp*correction/(Volume));
t=[0:1:200];

q=1.6e-19;

for i=1:length(leakage)
    n(i,:)=(n0-nleakage(i)*tao)*exp(-t/tao)+nleakage(i)*tao;
end

Pressure=(n*temperature*k/Volume)/133;
figure;
semilogy(t,Pressure,'.','MarkerEdgeColor','r');

xlabel('Pumping Time (second)')

ylabel('Pressure (Torr)')

title({'Pumping rate for the Field Ionization Pump',['array of
',int2str(emitters)],[num2str(leakage),' mm^3/s leak']})
% grid on;
 hold on;
```

References

[1] K. Ngyuen, L. Ludeking, J. Pasour, D. Pershing, E. Wright, D.K. Abe, B. Levush, "Design of a high-gain wideband high-power 220-Ghz multiple-beam serpentine TWT," *Vacuum Electronics Conference (IVEC), 2010 IEEE International*, May 2010.

[2] C.H.Aaronson, H.Amekura, Y. Sato, N. Kishimoto, "Vacuum fluorescent displays utilizing ZnO nanoparticles," *Journal of Applied Physics*, 109 (2), Jan. 2011.

[3] M. Esashi, "Wafer level packaging of MEMS," *Journal of Micromechanics and Microengineering*, 18 (7), May 2008.

[4] H.Zhou, H.Q. Li, V.Sharma, M.A. Schmidt, "A single-stage micromachined vacuum pump achieving 164 torr absolute presure," *Micro Electro Mechanical Systems (MEMS), 2011 IEEE 24th International Conference on*, pp. 1095-1098, Jan 2011.

[5] S. McNamara and Y.B. Gianchandani, "On-Chip Vacuum Generated by a Micromachined Knudsen Pump," *IEEE/ASME Journal of Microelectromechanical Systems*, 14 (4), pp. 741-746, Aug 2005.

[6] M. Doms, J. Muller, "A Micromachined Vapor-Jet Vacuum Pump," *Solid-State Sensors, Actuators and Microsystems Conference, Transducers 2007*, pp 2425-2428, Jun 2007.

[7] A. Gorecka-Drzazga, "Miniature and MEMS-type vacuum sensors and pumps," *Vacuum*, 83 (12), pp 1419-1426, Aug 2009.

[8] S.R. Green, Y.B. Gianchandani, "Miniature penning cell array for on-chip vacuum pumping," *Micro Electro Mechanical Systems (MEMS), 2011 IEEE 24th International Conference*, pp 1162-1165, Mar 2011.

[9] J-M. Bonard, M. Croci, C. Klinke, R. Kurt, O. Noury, N. Weiss, "Carbon nanotube films as electron field emitters," *Carbon*, 40 (10), pp 1715-1728, Aug 2002.

[10] A.-J. Cheng, D. Wang, H.W. Seo, C. Liu, M. Park, Y. Tzeng, "Cold cathodes for applications in poor vacuum and low pressure air environments: Carbon nanotubes versus ZnO nanoneedles," *Diamond and Related Materials*, 15 (2-3), pp 426-432, Mar 2006.

[11] A.M. Fennimore, L.T. Cheng, D. H. Roach, G. A. Reynolds, R. R. Getty, A. Krishnan, "Degradation of carbon nanotube field emitters driven by anode adsorbed water," *Appl, Phys. Lett.*, 92 (10), Mar 2008.

[12] C. Kimura, S. Kawai, K. Takizawa, Y. Horikawa, H. Aoki, T. Sugino, "Stable electron emission from BCN/carbon nanotube field emitter," *J. Vac. Sci. Technol. B*, 27 (2), pp 744-748, Mar 2009.

[13] Y. Yang, L. Liu, K. Jiang, S. Fan, "A vacuum sensor using field emitters made by multiwalled carbon nanotube yarns", *Vacuum*, 86 (7), pp 885-888, Feb 2012.

[14] D. Pflug, "Low Voltage Field Emitter Arrays through Aperture Scaling," PhD Thesis, MIT, 2000.

[15] B. J. Adeoti, "Field Ionization from Carbon NanoFibers," M.Eng. Thesis, MIT, Feb 2008.

[16] T. D. Mark, G. H. Dunn, *Electron Impact Ionization.* Springer, 1985.

[17] E. Hoffmann, V. Stroobant, *Mass Spectrometry: Principles and Applicatoins* West Sussez, England: John Wiley & Sons, 2002.

[18] R.P. Lattimer, H-R, Schulten, "Field Ionization and Field Desorption Mass Spectrometry: Past, Present, and Future" *Anal. Chem.*, 51, pp 1201A-1215A. Nov 1989.

[19] X. Guo, R.H. Fokkens, H.J.W. Peeters, N. M. M. Nibbering, Chris G. de Koster, "Multiple cationization of polyethylene glycols in field desorption mass spectrometry: a new approach to extend the mass scale on sector mass spectrometers," *Rapid Commun. Mass Spectrom.* 13 (21), pp 2223-2226, Oct 1999.

[20] T.M. Schaub, C.L. Hendrickson, J.P. Quinn, R.P. Rodgers, A.G. Marshall, "Instrumentation and Method for Ultrahigh Resolution Field Desorption Ionization Fourier Transform Ion Cyclotron Resonance Mass Spectrometry of Non-Polar Species," *Anal. Chem.*, 77 (5), pp 1317-1324, Feb. 2005

[21] J. H. Gross, *Mass Spectrometry: A textbook* Berlin: Springer-Verlag, 2004.

[22] P. J. Derrick, A. J . B. Robertson, "The Determination of the Kinetics of Unimolecular Ionic Dissociations by Field Ionization Mass Spectrometry with the Use of a Sharp Edge," *Proceedings of the Royal Society A*, 324 (1559), pp 491-502, Sep 1971.

[23] L. Liao, H. B. Lu, M. Shuai, J. C. Li, Y. L. Liu, Liu, Z. X. Shen, T. Yu, "A novel gas sensor based on field ionization from ZnO nanowires: moderate working voltage and high stability," *Nanotechnology*, 19 (17), Mar 2008.

[24] L.Y. Chen, "Double-gated Isolated Vertically Aligned Carbon Nanofiber Field Emission and Field Ionization Arrays," PhD Thesis, MIT, 2007.

[25] R.B. Sadeghian, M. S. Islam, "Ultralow-voltage field-ionization discharge on whiskered silicon nanowires for gas-sensing applications," *Nature Materials*, 10, pp 135-240, Jan 2011.

[26] M. Shiraishi, K. Hinokuma, M. Ata, "The measurement of work function of carbon nanotubes," *AIP Conf. Proc.* 544, pp. 359-362, Mar 2000.

[27] P. Liu, Q. Sun, F. Zhu, K. Lius, K. Jiang, L. Liu, Q. Li, S. Fan, "Measuring the work function of carbon nanotubes with thermionic method," *Nano Lett.*, 2008, 8 (2), pp 647-651, Jan 2008.

[28] R. Gomer, *Field Emissions and Field Ionization*, Harvard University Press, Cambridge MA, 1961.

[29] H. D. Beckey, "Principles of Field Ionization and Field Desorption Mass Spectrometry," *Pergamon Press*, London, 1977.

[30] R.L. Park, M.G. Lagally, *Solid State Phsics: Surfaces: Methods of Experimental Physics* Volume 22, Academic Press, London, 1985.

[31] K.L. Ghatak, *Techniques and Methods in Biology*, PHI Learning, 2010.

[32] M.M. Bursey, T. D. Williams, "Mass spectrometry," *AccessScience*, McGraw-Hill Companies, 2008.

[33] A. von Engel, *Ionized Gases*, Oxford University Press, London, Great Britain, 1965.

[34] S. Iijima, "Helical microtubules of graphitic carbon," *Nature* 354, pp 56-58, Nov 1991.

[35] R. J. Chen, S. Bangsaruntip, K. A. Drouvalakis, N. W. Shi Kam, M. Shim, Y. Li, W. Kim, P. J. Utz, H. Dai, "Noncovalent functionalization of carbon nanotubes for highly specific electronic biosensors," *Proc. Natl. Acad. Sci.* 100 (9), pp 4984-4989, Apr 2003.

[36] C. R. Martin, P. Kohli, "The emerging field of nanotube biotechnology," *Nature Reviews Drug Discovery*, 2, pp 29-37, Jan 2003.

[37] M. Endo, M. S. Strano, P. M. Ajayan, "Potential Applications of Carbon Nanotubes," *Top. Appl. Phys.*, 111 (13), 2008.

[38] W.A. de Heer, A. C. D. Ugarte, "A carbon nanotube field-emission electron source," *Science*, 270 (5239), pp 1179-1180, Nov 1995.

[39] H. Y. Choi, W. S. Chang, H. S. Kim, Y. H. Park, J. U. Kim, "Acquisition of X-ray images by using a CNT cold emitter," *Phys. Lett. A*, 357 (1), pp 36-41, May 2006.

[40] G. Hasko, and H. Ahmed, *J. Vac. Sci. Technol. B* 21, 693 (2003).

[41] Y. C. Kim, E. H. Yoo, "Printed Carbon Nanotube Field Emitters for Backlight Applications," *Jpn. J. Appl. Phys.*, 44 (15), pp. L454-456, Mar 2005.

[42] S. Fan, M. G. Chapline, N. R. Franklin, T. W. Tombler, A. M. Cassell, H. Dai, "Self-Oriented Regular Arrays of Carbon Nanotubes and Their Field Emission Properties," *Science*, 283 (5401), pp 512-514, Dec 1999.

[43] S.C. Sun, M.H.Tsai, "Effect of rapid thermal annealing of the electrical and physical properties of metalorganic chemical-vapor-deposited TiN," *Appl. Phys. Lett.*, 68 (5), Nov 1995.

[44] H.N. Cho, R.M. Su, H.J. Bae, J.H.Lee, C.W. Chung, "High Density Plasma Etching of Nickel Thin Films Using a Cl2/Ar Plasma," *J. Ind. Eng. Chem.*, 13 (6), pp 939-943, July 2007.

[45] R.C. Smith, S.R.P. Silva, "Maximizing the electron field emission performance of carbon nanotube arrays," *Appl. Phys. Lett.*, 94 (13), 2009.

[46] J.S.Suh, K.S.Jeong, J.S. Lee, I. Han, "Study of the field-screening effect of highly ordered carbon nanotube arrays," *Appl. Phys. Lett.*, 80 (13), Apr 2002.

[47] C. A. Deline, H. R. Goldberg, D. P. Morris, R. A. Ramos, "Field emission cathodes used in the FEGI get away special shuttle mission," *40th AIAA/ASME/SAE/ASEE Joint Propulsion Conference and Exhibit*, Jul 2004.

[48] C. A. Deline, T. M. Liu, D. P. Morris, B. E. Gilchrist, "Demonstration of field emission cathode operation in a plasma environment," *41st AIAA/ASME/SAE/ASEE Joint Propulsion Conference & Exhibit*, Jul 2005.